Site U1525[1]

R.M. McKay, L. De Santis, D.K. Kulhanek, J.L. Ash, F. Beny, I.M. Browne, G. Cortese, I.M. Cordeiro de Sousa, J.P. Dodd, O.M. Esper, J.A. Gales, D.M. Harwood, S. Ishino, B.A. Keisling, S. Kim, S. Kim, J.S. Laberg, R.M. Leckie, J. Müller, M.O. Patterson, B.W. Romans, O.E. Romero, F. Sangiorgi, O. Seki, A.E. Shevenell, S.M. Singh, S.T. Sugisaki, T. van de Flierdt, T.E. van Peer, W. Xiao, and Z. Xiong[2]

1. Background and objectives

Site U1525 is located on the continental slope at 75°0.0603′S, 173°55.2028′W in 1776 m of water on the southwestern levee of the Hillary Canyon in a depositional setting similar to that of Site U1524 (~87 km to the northeast) (Figure **F1**). Site U1525 is closer to the continental shelf edge, which is ~60 km southwest of the site, and the mouths of the Pennell and Glomar Challenger Basins. The levee shows asymmetric flanks, with a steep erosional flank (~500 m relief) facing the canyon to the northwest and a less-steep southeastern flank (30 m relief). The northeast flank sharply truncates parallel, high-amplitude reflectors outcropping at the seafloor, and in the
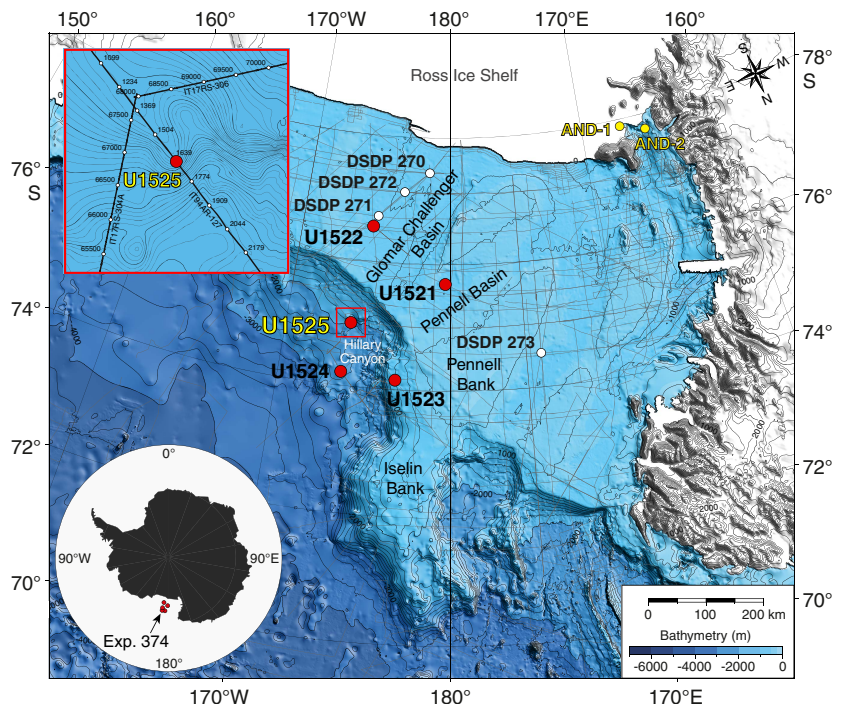
Contents

Supplementary Material

Figure F1. Bathymetric map with locations of Site U1525, other Expedition 374 sites, DSDP Leg 28 Sites 270–273, and ANDRILL Cores AND-1 and AND-2. Red box = location of inset map with Site U1525 on seismic-reflection Profile IT94AR-127 (Figure F2). Bathymetry from Arndt et al., 2013.

seismic-reflection profile chaotic seismic facies suggest that slope failure features affected the middle to lower units (Figure F2).

The Hillary Canyon is one of the largest conduits for newly formed Ross Sea Bottom Water (RSBW; a type of Antarctic Bottom Water [AABW]), which is focused in this channel by cascading dense water formed on the Ross Sea continental shelf passing down the continental rise (Bergamasco et al., 2002). The site also lies beneath the modern-day westward-flowing Antarctic Slope Current (ASC), which is thought to be stronger here than at the deeper water Site U1524 (Whitworth et al., 1998; Orsi and Wiederwohl, 2009). Seismic-reflection profiles indicate that the targeted sediments at Site U1525 are dominated by channel overspill and drift deposits characterized by stratified, parallel, high- to medium-amplitude seismic reflectors (Figure F2). Low-resolution multichannel seismic-reflection Profile IT94-127 (Figure F2) shows that the overall unit is stratified down to the acoustic basement at ~1 km below seafloor (3.5 s two-way traveltime [TWT]). Internal reflectors are spaced ~100 ms apart and are subparallel, laterally continuous, and subhorizontal. In the upper 50 m (0.7 s TWT), the reflectors onlap a highly angular unconformity that deepens and is likely older toward the southeast. These strata (green unit in Figure F2) are believed to be glacial debris flows interlayered with interglacial hemipelagic units of Pliocene to Pleistocene age that formed a prograding shelf margin fan at the mouth of the Glomar Challenger Basin coeval to or postdating Ross Sea Unconformity (RSU) 2.

The continental slope location of Site U1525 should allow for a more continuous assessment of oceanic forcings for (and response to) Antarctic Ice Sheet (AIS) variability than is possible from continental shelf records. The record of deposition at Site U1525 was anticipated to be primarily influenced by RSBW flowing down the Hillary Canyon but modified by an along-slope component associated with the westward-flowing ASC. Consequently, this site will enable assessment of the ocean drivers of ice
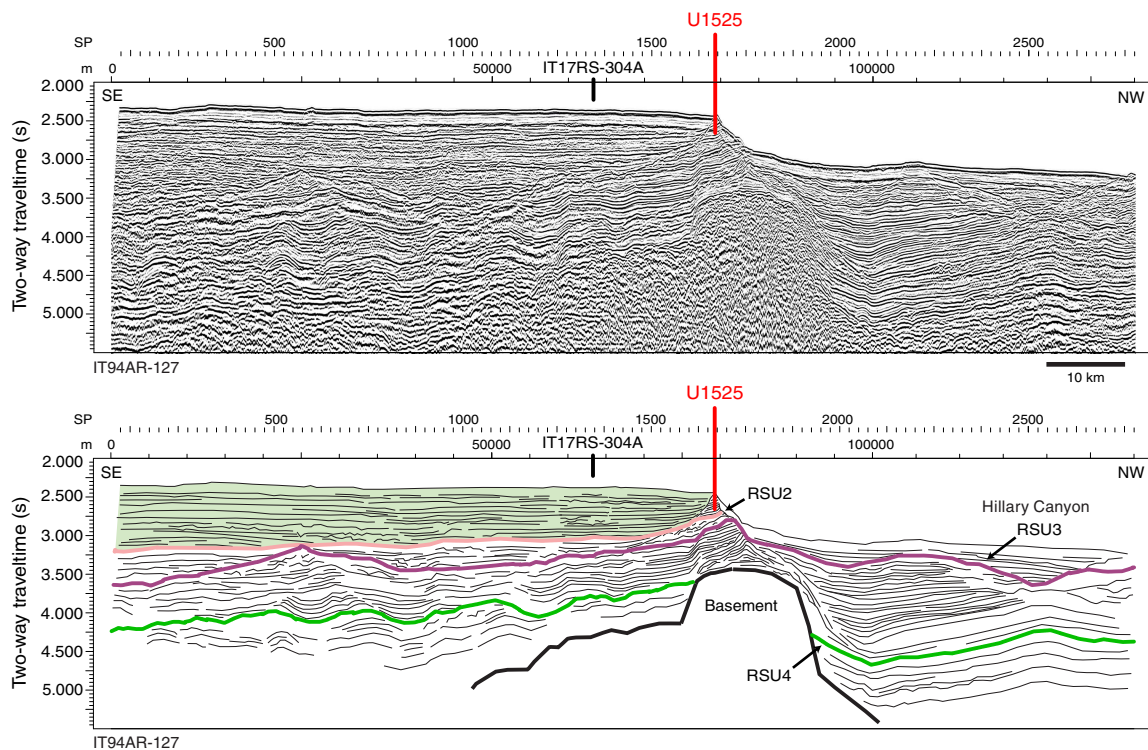
Figure F2. Top: multichannel seismic-reflection Profile IT94AR-127 across Site U1525 (see inset in Figure F1). Profile collected by Istituto Nazionale di Oceanografia e Geofisica Sperimentale (OGS, Italy) under Programma Nazionale delle Ricerche in Antartide (PNRA) in 1994 (Finetti et al., unpubl. data) with a 2 × 20 air gun (74.8 L). Data were acquired with a 1500 m streamer (120 channels; first offset = 164 m and last offset = 1664 m). The seismic reflection stack profile is available for scientific purposes through the Antarctic Seismic Data Library System. Reprocessing for Expedition 374 was done by Riccardo Geletti (OGS, unpubl.). SP = shot point. Bottom: interpretation of key seismic reflectors in Line IT94AR-127.

sheet variability and bottom water production (see Objective 2 in **Scientific objectives** in the Expedition 374 summary chapter [McKay et al., 2019b]). The direct record of RSBW flow down the Hillary Canyon obtained at Site U1525 could potentially be extrapolated to high-fidelity paleoceanographic records farther afield in the abyssal Pacific Ocean to better constrain the Antarctic influences on the global oceanic deep circulation. The Hillary Canyon is also a main route for glacial sediments being eroded and transported by ice streams from the innermost continental shelf to its edge, and provenance studies of the terrigenous sediment may allow for identification of changing ice sheet drainage pathways through the Neogene and Quaternary.

Ice-rafted debris (IRD) could be sourced by icebergs from the Ross Sea or transported from the east by the ASC, providing a proxy for dynamic ice discharge from the Pacific Ocean coastline sector of the WAIS. Pelagic sediments would have been deposited during periods of high productivity or a lull in turbidity current–overspill deposition and will provide proxy records of surface water properties, including sea ice cover, sea-surface temperature, stratification, and salinity. These proxy records will enable an assessment of the magnitude of polar amplification during past warm climates (Objective 2) and the role of oceanic forcing on driving ice sheet fluctuations at those times (Objective 3). In addition, continuous deposition, anticipated at this site through much of the upper Neogene and Quaternary, will allow assessment of the orbital response of the WAIS and adjacent oceanic/biological system over a range of past climatic conditions (Objective 4). The upper Quaternary record in the uppermost 50 m of glacial strata can also shed light on the most recent ice sheet advances.

2. Operations

Site U1525 (proposed Site RSCR-03A) was added to the schedule when we were forced to temporarily leave Site U1524 because of encroaching sea ice. The operational plan for Site U1525 consisted of advanced piston corer (APC)/extended core barrel (XCB) coring in a single hole until sea ice moved away from Site U1524. Hole U1525A was cored to a total depth of 213.2 m drilling depth below seafloor (DSF) using a combination of APC, half-length APC (HLAPC), and XCB coring (Table **T1**). The XCB system was deployed in the upper part of the hole (43.0–55.7 m DSF) to core past an indurated interval. We then switched back to piston coring and continued to core using both the APC and HLAPC systems to 131.2 m DSF. After reaching HLAPC refusal, we continued coring with the XCB system to 213.2 m DSF. We terminated the hole at that depth after receiving confirmation that the sea ice was expected to clear from Site U1524 by the next day. The rig floor was secured for transit at 0535 h (local ship time; UTC + 13 h) on 9 February 2018 to return to Site U1524. A total of 51.25 h (2.1 days) was spent in Hole U1525.

We collected a total of 33 cores at Site U1525. The APC system was deployed 8 times, collecting 63.23 m of core (103%). The HLAPC system was deployed 14 times, recovering 52.64 m of core (92%). The XCB system was used 11 times and collected 42.83 m (45%) (Table **T1**).

2.1. Transit to Site U1525

The 50 nmi transit to Site U1525 was completed in 5.6 h at an average speed of 8.9 kt. A small deviation in course was required to navigate around sea ice. The vessel arrived at Site U1525 at 0200 h on 7 February 2018. The thrusters were lowered and secured at 0215 h, clearing the drill floor for operations. We did not deploy an acoustic positioning beacon at this site.

2.2. Hole U1525A

Operations for Hole U1525A began by preparing the APC/XCB bottom-hole assembly (BHA) and then lowering the drill string toward the seafloor. The calculated precision depth recorder depth for the site was 1790.8 m drilling depth below rig floor (DRF). We picked up the top drive and lowered the drill bit to tag the seafloor. Because the tag indicated that the seafloor was soft, we prepared a nonmagnetic APC

Table T1. Core summary, Site U1525. CSF = core depth below seafloor, DRF = drilling depth below rig floor, DSF = drilling depth below seafloor. APC = advanced piston corer, HLAPC = half-length APC, XCB = extended core barrel. Core type: H = APC, F = HLAPC, X = XCB. Icefield = Icefield MI-5 core orientation tool. **Download table in CSV format.**

Hole U1525A

Latitude: 75°0.0603′S
Longitude: 173°55.2028′W
Water depth (m): 1775.74
Date started UTC (h): 6 February 2018, 1315
Date finished UTC (h): 8 February 2018, 1635
Time on hole (days): 2.14
Seafloor depth DRF (m): 1786.9
Seafloor depth calculation method: APC calculated
Rig floor to sea level (m): 11.16
Drilling system: 11-7/16 inch APC/XCB DB297
Penetration DSF (m): 213.2
Cored interval (m): 213.2
Recovered length (m): 158.7
Recovery (%): 74
Total cores (no.): 33
APC cores (no.): 8
HLAPC cores (no.): 14
XCB cores (no.): 11
Age of oldest sediment cored: Pleistocene

			Depth DSF (m)			Depth CSF (m)						
Core	Date	Time on deck UTC (h)	Top of interval	Bottom of interval	Interval advanced (m)	Top of cored interval	Bottom of cored interval	Length of core recovered (m)	Length of core curated (m)	Recovery (%)	Sections (N)	Comments
374-U1525A-												
1H	6 Feb 2018	2120	0.0	8.6	8.6	0.0	8.62	8.62	8.62	100	7	Icefield; mechanical shear
2H	6 Feb 2018	2220	8.6	18.1	9.5	8.6	18.77	10.17	10.17	107	8	Icefield
3H	6 Feb 2018	2310	18.1	27.6	9.5	18.1	28.21	10.11	10.11	106	8	Icefield
4H	7 Feb 2018	0015	27.6	28.9	1.3	27.6	28.91	1.31	1.31	101	2	Icefield; partial stroke
5F	7 Feb 2018	0115	28.9	33.6	4.7	28.9	33.80	4.90	4.90	104	5	
6F	7 Feb 2018	0150	33.6	38.3	4.7	33.6	38.54	4.94	4.94	105	5	
7F	7 Feb 2018	0220	38.3	43.0	4.7	38.3	38.92	0.62	0.62	13	2	Partial stroke
8F	7 Feb 2018	0310	43.0	43.0	0.0	43.0	43.00	0.00	0.00	0	0	Partial stroke; replace inner and outer core barrel seals; shattered liner
9X	7 Feb 2018	0450	43.0	51.0	8.0	43.0	43.00	0.00	0.00	0	0	
10X	7 Feb 2018	0540	51.0	55.7	4.7	51.0	51.33	0.33	0.33	7	1	Shattered liner; pumped out
11F	7 Feb 2018	0620	55.7	60.4	4.7	55.7	60.59	4.89	4.89	104	5	Replace piston seals
12F	7 Feb 2018	0730	60.4	65.1	4.7	60.4	65.51	5.11	5.11	109	5	
13F	7 Feb 2018	0805	65.1	69.8	4.7	65.1	69.78	4.68	4.68	100	5	Broken liner
14F	7 Feb 2018	0850	69.8	74.5	4.7	69.8	74.73	4.93	4.93	105	5	
15F	7 Feb 2018	0950	74.5	79.2	4.7	74.5	78.21	3.71	3.71	79	4	
16H	7 Feb 2018	1025	79.2	88.7	9.5	79.2	88.91	9.71	9.71	102	8	Icefield
17H	7 Feb 2018	1110	88.7	98.2	9.5	88.7	98.67	9.96	9.97	105	8	Icefield
18H	7 Feb 2018	1205	98.2	107.7	9.5	98.2	107.32	9.16	9.12	96	7	Icefield
19H	7 Feb 2018	1255	107.7	111.8	4.1	107.7	111.89	4.19	4.19	102	4	Icefield; partial stroke
20F	7 Feb 2018	1400	111.8	116.5	4.7	111.8	116.67	4.87	4.87	104	5	
21F	7 Feb 2018	1435	116.5	121.2	4.7	116.5	121.10	4.60	4.60	98	4	
22F	7 Feb 2018	1515	121.2	125.9	4.7	121.2	125.73	4.53	4.53	96	4	
23F	7 Feb 2018	1550	125.9	130.6	4.7	125.9	130.08	4.18	4.18	89	4	
24F	7 Feb 2018	1625	130.6	131.2	0.6	130.6	131.28	0.68	0.68	113	2	Partial stroke
25X	7 Feb 2018	1745	131.2	137.2	6.0	131.2	138.16	6.96	6.96	116	6	
26X	7 Feb 2018	1915	137.2	146.7	9.5	137.2	137.20	0.00	0.00	0	0	
27X	7 Feb 2018	2015	146.7	156.2	9.5	146.7	153.92	7.22	7.22	76	6	
28X	7 Feb 2018	2130	156.2	165.7	9.5	156.2	157.39	1.19	1.19	13	2	Shattered liner; pumped out
29X	7 Feb 2018	2305	165.7	175.2	9.5	165.7	167.30	1.60	1.60	17	2	Shattered liner; pumped out
30X	8 Feb 2018	0035	175.2	184.7	9.5	175.2	184.74	9.54	9.54	100	8	
31X	8 Feb 2018	0155	184.7	194.2	9.5	184.7	194.43	9.73	9.73	102	9	Shattered liner; pumped out
32X	8 Feb 2018	0335	194.2	203.7	9.5	194.2	195.89	1.69	1.69	18	3	Shattered liner; pumped out
33X	8 Feb 2018	0515	203.7	213.2	9.5	203.7	208.27	4.57	4.57	48	4	Shattered liner
		Hole U1525A totals:	213.2					158.70		74	148	

core barrel and positioned the drill bit at 1786 m DRF. Hole U1525A was started at 1000 h on 7 February 2018. Core 374-U1525A-1H recovered 8.62 m of sediment, establishing a seafloor depth of 1776 meters below sea level. We continued to core with the APC system with nonmagnetic core barrels through Core 4H (28.9 m DSF), which was a partial stroke. We switched to the HLAPC system to collect Cores 5F through 8F (28.9–43.0 m DSF). Because Core 8F was a partial stroke with no recovery, we switched to the XCB system to cut Cores 9X and 10X (43.0–55.7 m DSF) to penetrate an indurated zone. We then switched back to the HLAPC system for Cores 11F through 15F (55.7–79.2 m DSF). With continued successful piston coring, we switched back to full-length APC core barrels and collected Cores 16H through 19H, which penetrated to 111.8 m DSF. Because Core 19H recorded a partial stroke, we advanced 4.1 m based on recovery and returned to the HLAPC system, collecting Cores 20F through 24F (111.8–131.2 m DSF). Core 24F also recorded a partial stroke, indicating HLAPC refusal. We switched to the XCB coring system for the remainder of the hole, cutting Cores 25X through 33X to a total depth of 213.2 m DSF. We experienced multiple shattered core liners (6 out of 11; 55%), which we suspect resulted from a combination of very cold seawater (−1.7°C) circulating through the drill string and the small space between the core liner and the core barrel, which allows vibration of the core liner. Ice conditions at Site U1524 were forecast to improve over the next 24 h, so we opted to terminate coring after Core 33X. We pulled the drill string out of the hole, clearing the seafloor at 2150 h on 8 February. After conducting routine rig maintenance (slip and cut 115 ft of drill line), the remainder of the drill string was retrieved, and the rig floor was secured at 0535 h on 9 February, ending operations at Site U1525. The total time spent at Site U1525 was 51.25 h (2.1 days).

Total recovery in Hole U1525A was 158.70 m over 213.2 m of coring (74%). The APC coring system was deployed 8 times, collecting 63.23 m of core over 61.5 m of coring (103%). The HLAPC was deployed 14 times, collecting 52.64 m of core over 57.0 m of coring (92%). The XCB was deployed 11 times, recovering 42.83 m of core over 94.7 m of coring (45%) (Table **T1**).

3. Lithostratigraphy

Site U1525 includes a single hole cored to 213.2 m DSF. The 158.70 m of sediment recovered from Site U1525 is divided into three lithostratigraphic units (Table **T2**). A lithologic summary of Hole U1525A is shown in Figure **F3**. The dominant facies throughout the hole are diatom-bearing/rich mud and muddy diatom ooze interbedded on the decimeter to meter scale with diatom-bearing/rich mud/sandy mud with dispersed to abundant clasts and muddy diamict (Table **T3**). The lithologic succession at Site U1525 consists of sandy mud with dispersed clasts and diamict in the upper 51.11 m core depth below seafloor, Method A (CSF-A) (Unit I), which overlies a 62.88 m thick sequence of interbedded massive/bioturbated diatom-bearing/rich mud and diatom-bearing/rich mud with silt laminae (Unit II). The lowermost 42.5 m consists of diatom-rich mud and muddy diatom ooze with fine laminae of silt and bioturbated

Table T2. Lithostratigraphic units, Hole U1525A. **Download table in CSV format.**

| Unit/ Subunit | Top | | Bottom | | Basic description | Age | Recovery (%) |
	Core, section, interval (cm)	Depth CSF-A (m)	Core, section, interval (cm)	Depth CSF-A (m)			
I	374-U1525A- 1H-1, 0	0	374-U1525A- 10X-1, 11	51.11	Massive diatom-bearing sandy mud with dispersed clasts interbedded with clast-poor/rich muddy diamict	Pleistocene	80
IIA	10X-1, 11	51.11	18H-1, 0	98.20	Massive to laminated diatom-bearing mud interbedded with diatom-bearing sandy mud with dispersed clasts	Pleistocene	92
IIB	18H-1, 0	98.20	21F-2, 58	118.58	Massive to laminated diatom-rich mud interbedded with diatom-rich sandy mud with dispersed clasts	Pleistocene	100
III	21F-2, 58	118.58	33X-CC, 34	208.27	Massive to finely laminated muddy diatom ooze/diatom-rich mud interbedded with diatom-rich sand and diamict	Pleistocene	58
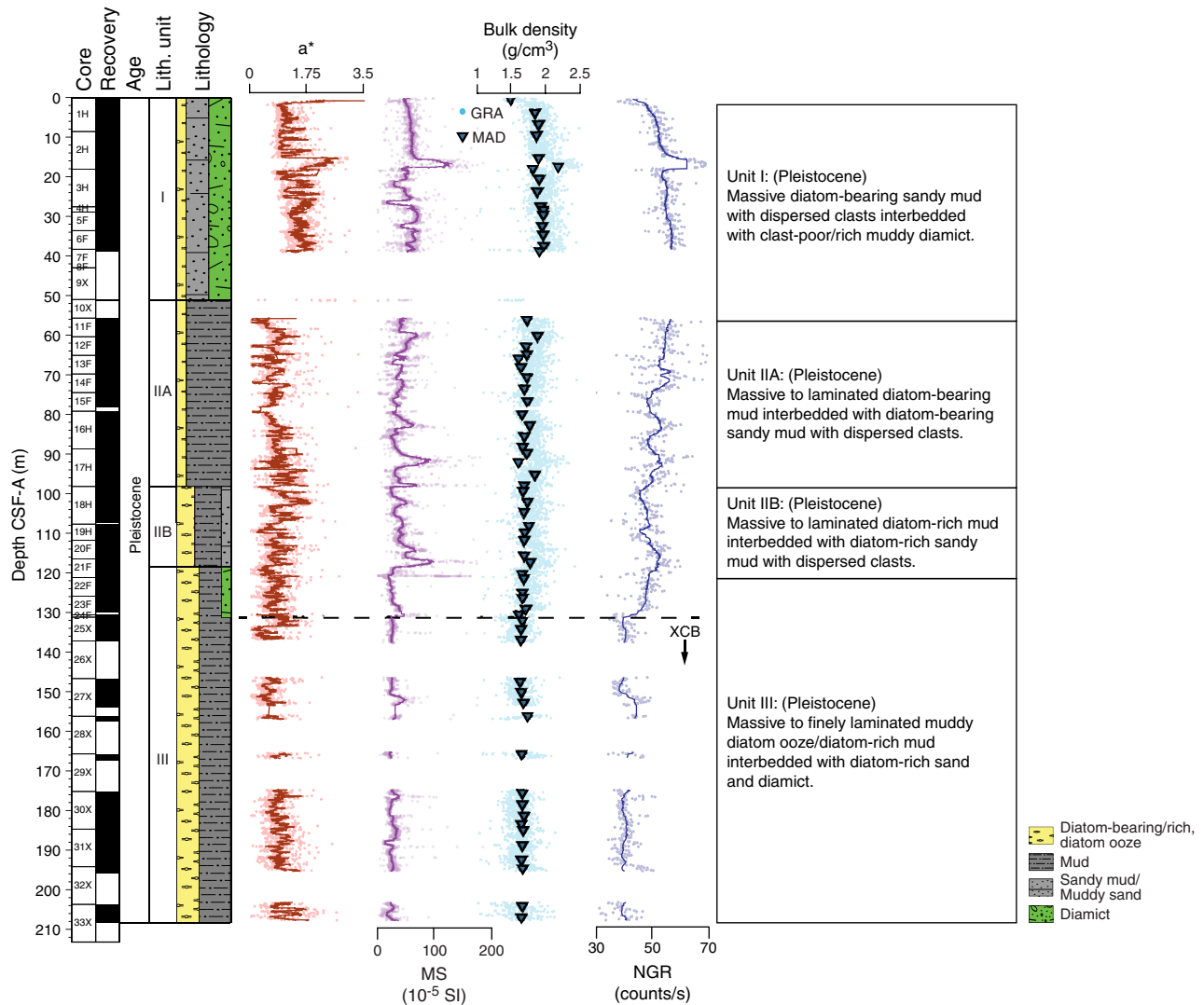
Figure F3. Lithostratigraphic summary, Hole U1525A. GRA = gamma ray attenuation, MAD = moisture and density, magnetic susceptibility (MS), and natural gamma radiation (NGR) are shown with a 50-point running median equivalent to 1.25 and 5 m, respectively.

Table T3. Observed facies, Hole U1525A. **Download table in CSV format.**

Continental rise facies	Additional facies information	Lithostratigraphic unit/subunit	Tentative depositional environment/diagenesis
1r: massive to stratified diamict	Clast-rich to clast-poor sandy to muddy diamict. Biogenic silica content varies from diatom-bearing to diatom-rich. Clasts are subangular to subrounded, sometimes faceted, poorly sorted, aligned in some intervals, and contain a range of lithologies. Stratification is weak to well defined. Bioturbation and shell fragments are common.	I, IIB, III	Ice-proximal glaciomarine, mass flow deposits, suspension settling, ice rafting, winnowing/redeposition by currents
2r: mud	Massive to laminated mud to diatom-bearing mud. Laminae are defined by color, particle size (i.e., silt and sand), and/or biogenic content and range from planar to wavy and discontinuous. Bioturbation intensity varies. Soft-sediment deformation and postdepositional structures are common.	IIA, IIB, III	Ice-distal open marine, sediment gravity flows, winnowing/redeposition by currents
3r: diatom-rich mud/diatom ooze	Bioturbated to laminated diatom-rich mud(stone) and diatom ooze with dispersed to common clasts. Similar to Facies 3r of Site U1524, with >50% diatoms.	I, IIB, III	Ice-distal open marine, ice rafting, sediment gravity flows
4r: sand	Massive bioturbated decimeter-scale sand beds with diatoms and foraminifers. Dispersed clasts are common and vary in size and angularity.	IIA	Ice-proximal glaciomarine, mass flow deposits, winnowing/redeposition by currents

diatom-rich sandy diamict (Unit III). Photographs of primary lithologies, sedimentary structures, and accessories are shown in Figures **F4** and **F5** and summarized in Figure **F6**, which highlights lithologic variations and trends based on data distilled from DESClogik.
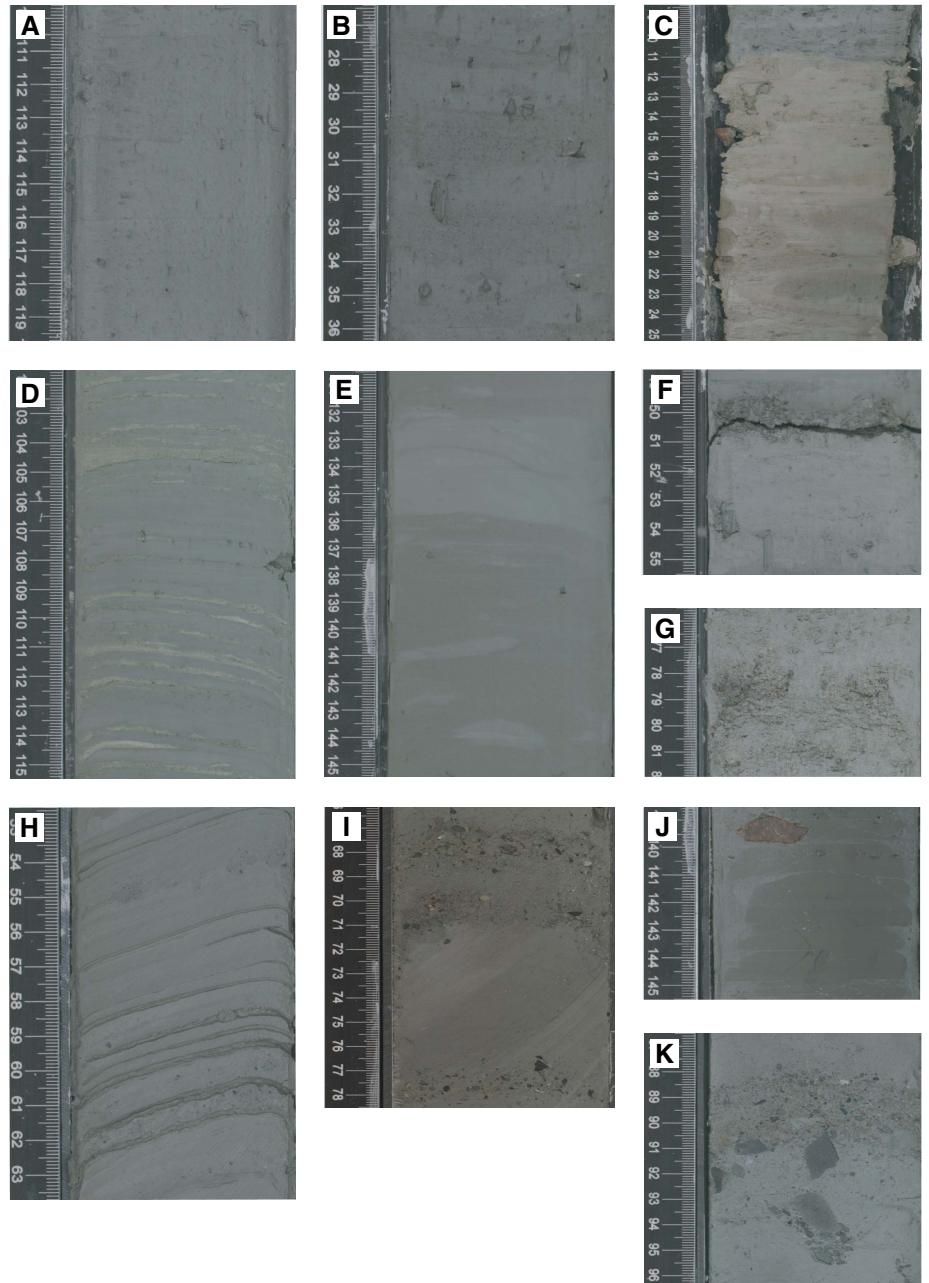

Figure F4. Primary lithologies, Hole U1525A. A. Diatom-bearing/rich sandy mud (Unit I; 2H-1A, 110–119 cm). B. Muddy diamict (Unit I; 5H-4A, 27–36 cm). C. Diatom-bearing/rich mud overlain by muddy diamict (Unit I/II contact; 10X-1A, 9–25 cm). D. Diatom-bearing mud with silty sand laminations (Subunit IIA; 17H-4A, 102–115 cm). E. Bioturbated diatom-bearing mud (Subunit IIA; 13H-1A, 131–145 cm). F. Diatom-bearing mud with clasts (Subunit IIA; 17H-6A, 49–55 cm). G. Foraminifer-bearing sand (Subunit IIA; 17H-4A, 76–82 cm). H. Diatom-rich mud with silt laminations (Subunit IIB; 20F-2A, 53–63 cm). I. Contact between diatom-bearing/rich mud and diatom-bearing sandy diamict (Subunit IIB; 18F-3A, 67–78 cm). J. Diatom-rich mud (Unit III; 27X-4A, 139–145 cm). K. Sandy mud to diamict (Unit III; 22F-2A, 87–96 cm).

3.1. Unit descriptions

Site U1525 is divided into three lithostratigraphic units (I–III; youngest to oldest) based on lithologic changes observed downhole (Figure **F3**). The units were determined using a combination of visual core description, microscopic examination of smear slides, and color spectral observations (see **Lithostratigraphy** in the Expedition 374 methods chapter [McKay et al., 2019a]). Unit II is divided into two subunits (IIA and IIB; youngest to oldest).
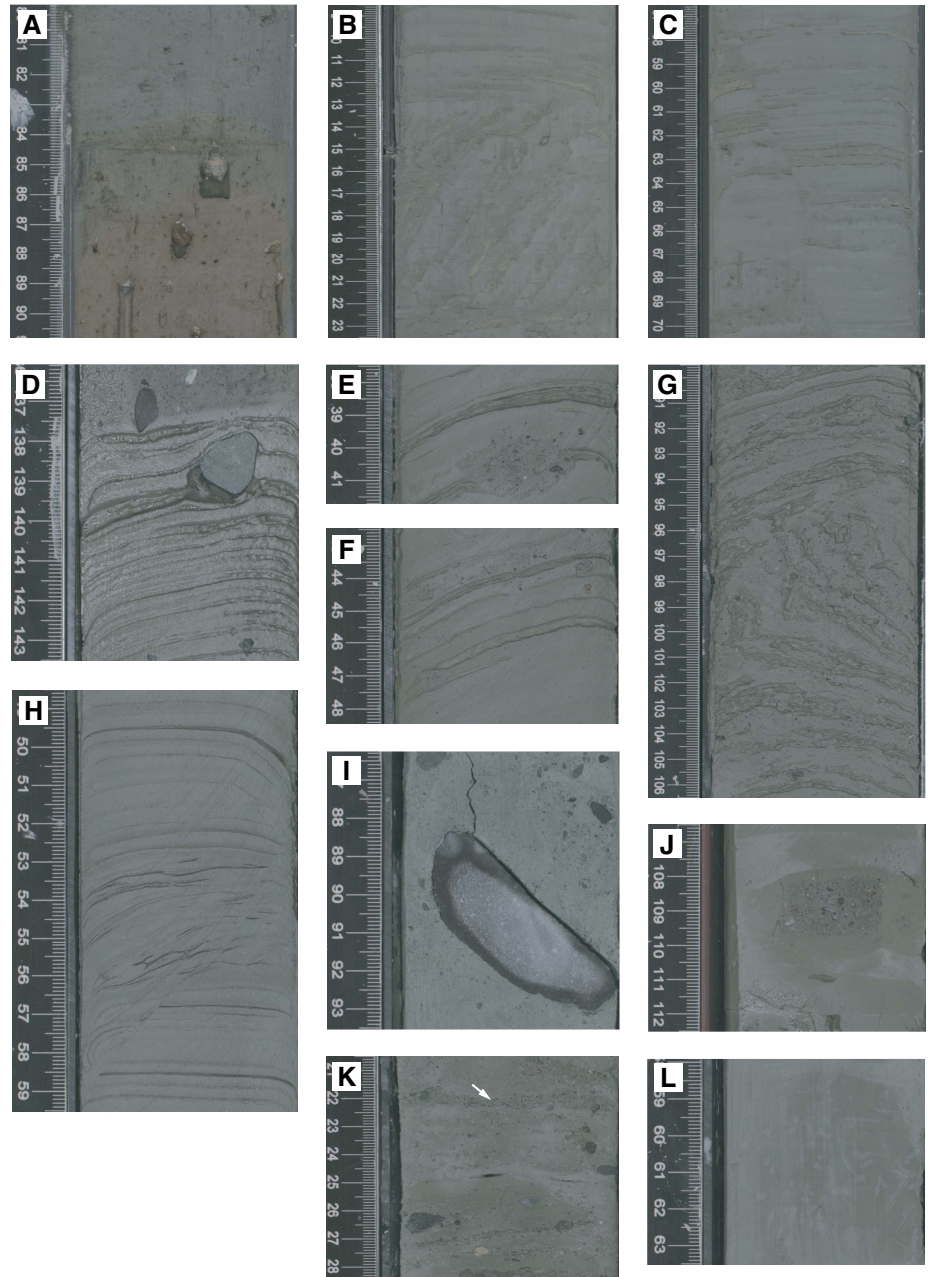

Figure F5. Sedimentary structures and lithologic accessories, Hole U1525A. A. Gradational contact from diatom-bearing clast-poor muddy diamict (upsection) to clast-rich muddy diamict (Unit I; 2H-5A, 80–91 cm). B. Tilted laminations and soft-sediment deformation (Subunit IIA; 17H-2A, 9–23 cm). C. Postdepositional fault (Subunit IIA; 11F-3A, 57–70 cm). D. Draping and deformation of silt laminae in mud caused by clast (Subunit IIB; 21F-1A, 138–143 cm). E. Mud with silt laminations and diamict clast (Subunit IIB; 20F-2A, 38–41 cm). F. Mud with silt laminations (Subunit IIB; 20F-2A, 43–48 cm). G. Soft-sediment deformation of silt laminae in mud (Subunit IIB; 20F-2A, 90–106 cm). H. Faulted and deformed laminations (Unit III; 23F-3A, 49–59 cm). I. Faceted clast in diatom-rich diamict (Unit III; 30X-2A, 87–93 cm). J. Sandy diamict clast in mud (Unit III; 31X-7A, 107–112 cm). K. Sand stringer in diatom-rich diamict (Unit III; 22F-2A, 21–28 cm). L. Diatom-rich mud with bioturbation (Unit III; 30X-5A, 58–63 cm).

3.1.1. Unit I

Interval: 374-U1525A-1H-1, 0 cm, to 10X-1, 11 cm
Depth: 0–51.11 m CSF-A
Thickness: 51.11 m
Age: Pleistocene
Lithology: diamict, diatom-bearing sandy mud with dispersed clasts

Lithostratigraphic Unit I consists of unconsolidated massive bioturbated gray diatom-bearing/rich sandy mud with dispersed clasts interbedded on the meter scale
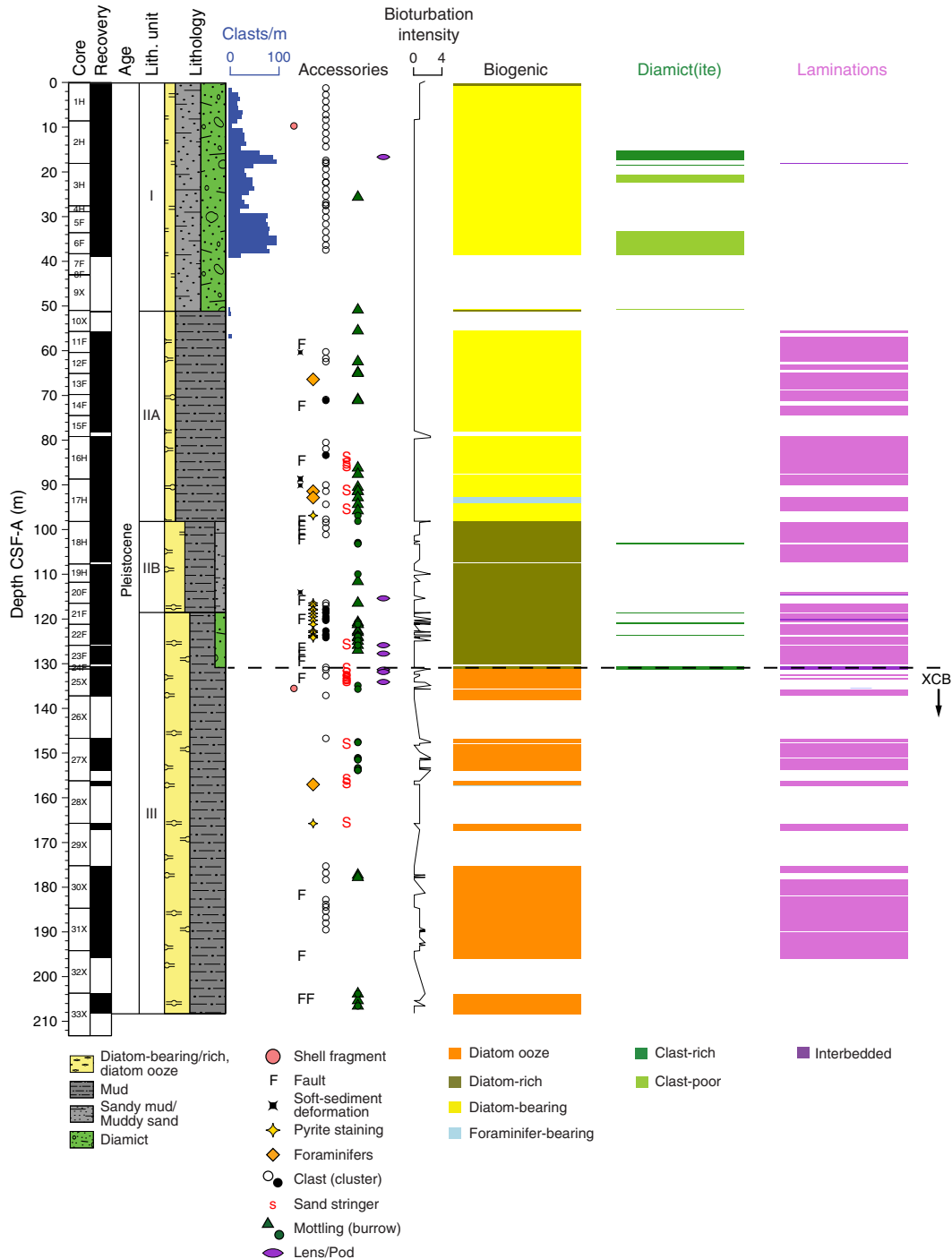

Figure F6. Lithology and sedimentary structures, Hole U1525A. Downhole profiles represent the occurrence of a described lithology or lithologic feature. Bioturbation intensity: 0 = no apparent bioturbation (<10%) to 4 = complete bioturbation (>90%).

with gray to light yellowish brown clast-poor/rich muddy diamict. Beds of diatom-bearing sandy mud with dispersed clasts (Figure **F4A**) are as thick as 8 m, and muddy diamict (Figure **F4B**) beds are as thick as 5 m. The beds are overcompacted (shear strength = 9.0 kg/cm^2; see **Physical properties**) and contain randomly distributed, subrounded to subangular igneous and metamorphic clasts. Bedding contacts are sharp or gradational (Figure **F5A**). The lower boundary of Unit I (interval 374-U1525A-10X-1A, 11 cm) (Figure **F4C**) is a sharp contact between diatom-bearing/rich mud and diamict. This contact is in an interval of poor recovery that, based on the presence of muddy diamict in Section 7F-1 and piston core refusal in Core 8F (see **Operations**), likely consists of compacted diamict. The base of the unit was cored with the XCB system, with zero recovery in Core 9X and poor recovery in Core 10X that includes the contact between Units I and II. Recovery in Unit I is 40.78 m (80%).

3.1.2. Unit II

Interval: 374-U1525A-10X-1, 11 cm, to 21F-2, 58 cm
Depth: 51.11–118.58 m CSF-A
Thickness: 67.47 m
Age: Pleistocene
Lithology: diatom-bearing/rich mud/sandy mud, diamict

Lithostratigraphic Unit II consists of massive greenish gray diatom-bearing/rich mud with dispersed clasts to diamict interbedded at the decimeter to meter scale with greenish gray diatom-bearing/rich mud containing silt and sand laminae. Unit II is divided into two subunits based on the structure and texture of laminations, very coarse sand and gravel clasts, centimeter-scale diamict beds, and diatom abundance (Figures **F3**, **F6**; Table **T2**). The lower contact of Unit II is defined by the increased thickness of bioturbated decimeter-scale sandy diamict beds, increased diatom content, and shifts in laminae frequency and clast content. Recovery in Unit II is 63.51 m (94%).

3.1.2.1. Subunit IIA

Interval: 374-U1525A-10X-1, 11 cm, to 18H-1, 0 cm
Depth: 51.11–98.20 m CSF-A
Thickness: 47.09 m
Age: Pleistocene
Lithology: diatom-bearing mud/sandy mud

Lithostratigraphic Subunit IIA consists of massive to laminated greenish gray to dark greenish gray diatom-bearing mud interbedded at the decimeter to meter scale with diatom-bearing mud/sandy mud with dispersed clasts. In Subunit IIA, a typical decimeter- to meter-scale sequence consists of diatom-bearing mud with fine sand and silt laminae with sharp lower contacts and internal normal grading overlain by diatom-bearing mud with thin, more discontinuous laminae. This sequence is overlain by massive bioturbated diatom-bearing mud/sandy mud with clasts (Figure **F4D–F4F**). Soft-sediment deformation features and microfaulting are observed in the laminated sequences (Figures **F5B, F5C**, **F6**). Intervals of decimeter-scale bioturbated foraminifer-bearing sandy mud with dispersed clasts and sharp upper and lower contacts occur in some of the massive diatom-bearing mud beds (e.g., Section 374-U1525A-17H-4A; Figures **F4G**, **F6**). The Subunit IIA/IIB boundary is defined by a distinct change in the nature of the laminated mud beds, an increase in diatom content, and improved preservation of whole diatom frustules below Core 17H. Recovery in Subunit IIA is 43.21 m (92%).

3.1.2.2. Subunit IIB

Interval: 374-U1525A-18H-1, 0 cm, to 21F-2, 58 cm
Depth: 98.20–118.58 m CSF-A
Thickness: 20.38 m

Age: Pleistocene
Lithology: diatom-rich mud/sandy mud, diamict

Lithostratigraphic Subunit IIB consists of laminated greenish gray diatom-rich mud (Figure **F4H**) interbedded at the decimeter to meter scale with massive bioturbated olive gray to greenish gray diatom-rich sandy mud with dispersed clasts and diamict beds (Figure **F4H, F4I**). The laminated diatom-rich mud beds are characterized by fine sand and silt laminae with sharp upper and lower contacts (Figure **F5E, F5F**) and internal planar to cross-bedding structures. Many laminated intervals contain coarse sand grains and gravel clasts that deform underlying silt laminae (Figure **F5D**). Clast composition varies and includes diamictite clasts. Sand pods, lenses, and stringers are observed, together with soft-sediment deformation (e.g., intervals 374-U1525A-20F-2A, 38–48 cm; 20F-2A, 90–106 cm; and 21F-1A, 137–143 cm; Figure **F5G**). Bioturbated diatom-rich sandy mud with dispersed clast beds sometimes contain sufficient clasts to be classified as muddy diamict. Recovery in Subunit IIB is 20.30 m (100%).

3.1.3. Unit III

Interval: 374-U1525A-21F-2, 58 cm, to 33X-CC, 34 cm
Depth: 118.58–208.27 m CSF-A
Thickness: 89.69 m
Age: Pleistocene
Lithology: diatom-rich mud to muddy diatom ooze, diatom-rich sandy mud, diamict

Lithostratigraphic Unit III consists of laminated greenish gray diatom-rich mud to muddy diatom ooze (Figure **F4J**) interbedded at the decimeter scale with massive bioturbated light greenish gray diatom-rich sandy mud to muddy diatom ooze with dispersed clasts and diamict (Figure **F4K**). Beds of diatom-rich mud with dispersed clasts are faintly laminated, defined by submillimeter- to millimeter-scale silt laminae and millimeter- to centimeter-scale color variations. Laminae have sharp upper and lower contacts and sometimes appear rhythmic (e.g., interval 374-U1525A-23F-3A, 58–135 cm). Biogenic silica estimates from smear slides are variable, but some intervals are compositionally defined as muddy diatom ooze. However, the abundance of diatom fragments exceeds that of whole or partially fragmented diatom frustules. Sand to silt laminae are similar to those observed in Subunit IIB, but outsized clasts are less common (Figure **F5I**). Laminae occur sporadically downhole to Core 33X and often exhibit soft-sediment deformation and postdepositional faulting (Figures **F5H, F6**). Coarse sand pods, lenses, and laminae occur throughout (Figure **F5J, F5K, F6**). The bioturbated diatom-rich sandy mud with dispersed clasts coarsens upward into centimeter-scale diamict beds with bioturbated lower contacts (Figures **F4K, F5L**). Recovery in Unit III is 54.41 m (58%).

3.2. Facies distribution

At Site U1525, four main lithofacies are identified based on common lithologic and textural characteristics (Table **T3**). Although there are textural similarities between the shelf and slope sites, the depositional processes operating on the slope and rise are different from those on the shelf (Sites U1521, U1522, and U1523); therefore, we use an "r" to distinguish the slope/rise facies from the shelf facies. The lithofacies at Site U1525 largely conform with Lithofacies 1r, 2r, and 3r described at Site U1524 (see **Lithostratigraphy** in the Site U1524 chapter [McKay et al., 2019c]) but with some notable differences. At Site U1525, Lithofacies 1r (massive to stratified diamict) also includes a massive, overcompacted, poorly sorted clast-rich muddy diamict with subangular to rounded clasts of diverse lithologies. In lithostratigraphic Unit I, this facies likely represents mass flow deposits with rainout from ice rafting. The character of the laminae in Facies 2r and 3r also differs. For example, some laminae contain internal structures and sharp upper contacts that indicate reworking by bottom currents.

One additional facies (4r; poorly sorted sand) is observed at Site U1525 and is described below.

3.2.1. Poorly sorted sand

Facies 4r consists of massive poorly sorted sand with dispersed clasts. This facies is diatom-bearing/rich and/or foraminifer-bearing/rich. Basal contacts are sharp, gradational, and/or bioturbated. Similar to the diamict facies, inverse grading is common. Facies 4r reflects sedimentation influenced by current winnowing, mass transport, and/or ice rafting.

3.3. Diagenesis

The presence of pyrite in laminated and bioturbated sediments indicates postdepositional diagenesis from bacterial decomposition of organic material in a sulfate-reducing environment.

3.4. Preliminary depositional interpretation

Coring at Site U1525 recovered a sequence of Pleistocene sediments from a channel levee complex on the upper continental slope of the Ross Sea. The depositional setting and lithostratigraphic units at Site U1525 reveal an interplay between downslope, along-slope (e.g., winnowing), hemipelagic, and pelagic processes. Clasts occur throughout, indicating the persistent influence of ice rafting. The mass transport deposits in lithostratigraphic Unit I may reflect changes in glacial dynamics on the outer continental shelf. Units II and III were deposited in a high-relief levee setting and therefore are influenced by the overspill of turbidity currents, winnowing by bottom currents, and ice rafting. Generally, siliciclastic content increases upsection. In Unit III, diatom fragments are observed in the diatom-rich mud/muddy diatom ooze intervals, suggesting that these deposits are not primary pelagic/hemipelagic ooze and mud. These sequences may be reworked from pelagic diatom ooze units originally deposited on the Ross Sea continental shelf or upper continental slope and subsequently transported downslope. In addition to downslope processes, internal structures in laminae and inverse grading of sand and diamict intervals in Units II and III may reflect winnowing related to temporal changes in the strength of the westward-flowing ASC. Thus, Site U1525 sediments record both down- and along-slope processes in a Pleistocene open-marine to glaciomarine environment.

4. Biostratigraphy and paleontology

Core catcher samples from Site U1525 were analyzed for siliceous (diatoms, radiolarians, silicoflagellates, and ebridians), calcareous (foraminifers and calcareous nannofossils), and organic (dinoflagellate cysts [dinocysts] and other aquatic palynomorphs, pollen, and spores) microfossils. Samples in the upper 111.84 m CSF-A (from Sample 374-U1525A-19H-CC and above) are either devoid of microfossils, contain only trace amounts, or include a "residual" assemblage of resistant forms that have likely been engaged in multiple phases of transport and reworking by ice and/or bottom currents. The character of this interval is defined by the abundance and persistence of reworked taxa (Table **T4**). These reworked specimens represent diatom taxa that were eroded and transported from discrete source beds of early Miocene, middle Miocene, and late Miocene to early Pliocene age into this interval at Site U1525. These older displaced diatoms co-occur in this interval with an assemblage of robust and heavily silicified diatoms. This combination likely reflects a concentration of taxa that survived multiple stages of transport and redeposition. This interval is problematic, and shipboard microfossil biostratigraphy is unable to resolve a reliable and defendable age profile with the ~5–10 m sample spacing available between core catchers. Future targeted sampling of intervals identified as having been deposited primarily by pelagic processes (e.g., interglacial intervals) in postcruise studies may provide additional age control. In this interval, Sample 4H-CC at 28.86 m CSF-A

Table T4. Diatom distribution, Hole U1525A. **Download table in CSV format.**

yields an age-diagnostic radiolarian event that indicates an age older than 0.65 Ma for this sample (Table **T5**; Figures **F7**, **F8**, **F9**).

Microfossils in samples deeper than 111.84 m CSF-A (e.g., Sample 374-U1525A-19H-CC) are more abundant and well preserved, and several age diagnostic radiolarians and diatoms were encountered. Although a small background presence of reworked diatoms continues in this interval with the persistent presence of *Thalassiosira oliverana* var. *sparsa* (a late Miocene to early Pliocene diatom), an expected sequence of early Pleistocene first appearance datum (FAD) and last appearance datum (LAD) events is evident (Figures **F7**, **F8**, **F9**). Dinocysts are sparse in this interval, and only Sample 27X-CC (153.87 m CSF-A) in the lower Pleistocene yields abundant dinocysts (Figure **F7**). The assemblage comprises species known from the uppermost Quaternary sediments of the Atlantic sector of the Southern Ocean, south of the Polar Front. Planktonic and benthic foraminifers are also most abundant and diverse in the mid-Pleistocene section, and the occurrences of the planktonic species *Globoconella inflata* at 88.86 m CSF-A (Sample 16H-CC) and *Globigerina bulloides* and *Globigerina falconensis* at 125.67 m CSF-A (Sample 22F-CC) indicate the presence of warmer-than-present water (Figure **F7**). A sparse Neogene assemblage of calcareous nannofossils is present in Sample 17H-3A, 82 cm (92.34 m CSF-A) (Figure **F7**).

4.1. Diatoms

All core catcher samples from Site U1525 were examined for diatoms, and their distribution is shown in Figures **F7** and **F9** and Table **T4**. Samples 374-U1525A-1H-CC to 19H-CC (8.57–111.84 m CSF-A) are inferred to be late Pleistocene in age, although few diatoms characteristic of this age are identified in this interval. Assemblages comprise a mixture of reworked Miocene, Pliocene, and Pleistocene diatoms (Table **T4**; Figures **F7**, **F9**), which makes age assignment for this interval difficult. These reworked taxa are generally heavily silicified and include a persistent presence of *T. oliverana* var. *sparsa* (total range = 8.6–4.9 Ma), *Trinacria* spp. (generally common at >4.5 Ma), *Stephanopyxis* spp. (generally common at >4.5 Ma), *Actinocyclus ingens* var. *nodus* (14.5–12.6 Ma), *Pseudammodocium lingii* (a Miocene ebridian lorica common in Ross Sea sediment cores), and other robust taxa *Paralia sulcata*, *Actinoptychus* spp., *Aulacodiscus brownei*, and *Coscinodiscus* spp. fragments. Although there are very likely discrete stratigraphic intervals in the upper ~111 m CSF-A of Site U1525 that contain in situ assemblages of diatoms and other microfossils that reflect primary marine deposition, none of these intervals were identified during shipboard investigations of core catcher samples. Postcruise selective sampling may allow the identifica-

Table T5. Diatom and radiolarian biostratigraphic events, Hole U1525A. Datum code: R = radiolarian, D = diatom, N = nannofossil. LAD = last appearance datum, FAD = first appearance datum. See Biostratigraphy and paleontology in the Expedition 374 methods chapter (McKay et al., 2019a) for an explanation of the different adopted ages. **Download table in CSV format.**

Age (Ma)	Code	Datum type	Species name	Depth range CSF-A (m) Top	Depth range CSF-A (m) Bottom	Core, section, interval (cm)	Depth CSF-A (m)
						374-U1525A-	
0.65	R1	LAD	*Antarctissa cylindrica*	28.21	28.86	4H-CC	28.86
1.73	N1	FAD	Absence of *Gephyrocapsa* spp. (>4 μm)	92.34	92.34	17H-3, 82	92.34
1.72	R2	LAD	*Cycladophora pliocenica*	107.32	111.84	19H-CC	111.84
1.9	D1	LAD	*Thalassiosira kolbei*	107.32	111.84	19H-CC	111.84
2.2	D2	LAD	*Actinocyclus maccollumii*	111.84	116.62	20F-CC	111.84
1.95	D3	LAD	*Actinocyclus fasciculatus*	111.84	116.62	20F-CC	111.84
2.35	R3	LAD	*Helotholus vema*	111.89	116.62	20F-CC	116.62
2.4	D4	LAD	*Rouxia diploneides*	116.67	121.05	21F-CC	121.05
2.2	D5	LAD	*Thalassiosira vulnifica*	121.05	125.67	22F-CC	125.67
2.47	R4	LAD	*Desmospyris spongiosa*	130.08	131.22	24F-CC	131.22
2.5	D6	FAD	*Rouxia leventerae*	153.87	157.34	27X-CC	157.34
2.7	D7	FAD	*Actinocyclus fasciculatus*	208.22	208.27	33X-CC	208.27
2.8	D8	FAD	*Actinocyclus maccollumii*	208.22	208.27	33X-CC	208.27

tion of sedimentological facies where initial diatom production and final deposition ages are closely aligned, which may provide better age control through this interval.

The following discussion focuses on the lower half of Site U1525, which is interpreted to represent hemipelagic to pelagic environments. Some intervals record high diatom production in overlying water, and in other intervals diatoms were likely brought to the site by ocean currents with local modification and/or concentration of the diatom assemblage. Although diatom abundance is high in many intervals, diatoms are often present as finely fragmented remains and make up a large component of the clay-sized fraction of Site U1525 sediments.

Figures **F7** and **F9** present biostratigraphic datum events identified at Site U1525 that indicate age and zonal assignments. The top of the *Thalassiosira kolbei* Zone is identified by the last appearance of *T. kolbei* (1.9 Ma) in Sample 374-U1525A-19H-CC (111.84 m CSF-A). A disconformity is indicated between Samples 19H-CC and 20F-CC (between 111.84 and 116.52 m CSF-A), as indicated by biostratigraphic and magnetic polarity reversal constraints (Figure **F8**), which removed part of the *T. kolbei* Zone. The LADs of two distinctive diatoms are noted in this zone, *Actinocyclus fasciculata* (LAD at 1.95 Ma) and *Actinocyclus maccollumi* (LAD at 2.2 Ma) in the lower portion of the *T. kolbei* Zone in Sample 20F-CC (116.62 m CSF-A). These species are
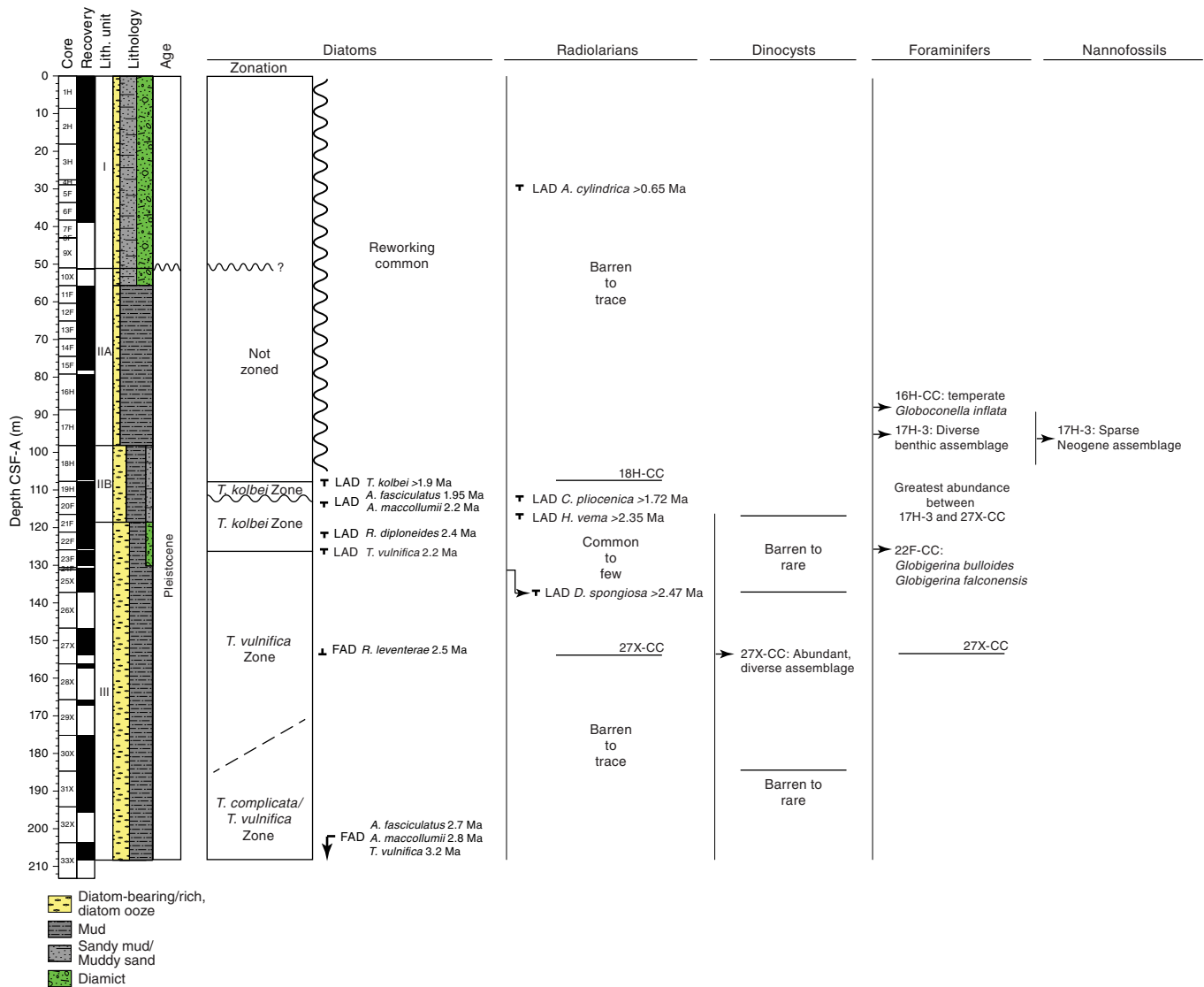

Figure F7. Micropaleontology summary, Hole U1525A. Diatom and radiolarian biostratigraphic zonations are defined by the first appearance datum (FAD) and/or last appearance datum (LAD) of corresponding marker species.

present downhole through the rest of the lower Pleistocene section at Site U1525, including the underlying *T. vulnifica* Zone, the top of which is identified by the LAD of *T. vulnifica* in Sample 22F-CC (125.67 m CSF-A).

A single occurrence of *Rouxia leventerae* (FAD at 2.5 Ma), noted in Sample 374-U1525A-27X-CC (153.87 m CSF-A), suggests an age of <2.5 Ma for this level. A rich and well-preserved assemblage of *Rouxia* spp., *Fragilariopsis* spp., and many spines and girdle bands of *Corethron pennatum* are also noted in Sample 27X-CC, revealing an interval of productive pelagic sedimentation at this site, with preservation of fine, lightly silicified diatoms.

The lower boundary of the *T. vulnifica* Zone and the upper boundary of the underlying *Thalassiosira complicata/T. vulnifica* Zone was not identifiable at Site U1525 because of the persistent reworking of *T. complicata* throughout this interval that prevents a clear identification of its highest occurrence, which defines this boundary. In the Ross Sea during Expedition 374, we use the LAD of *T. complicata* in place of the LAD of *Thalassiosira insigna*, whose LAD is used in the Southern Ocean biostratigraphic framework to define the top of the *T. insigna/T. vulnifica* Zone. For our use during Expedition 374, we recognize the LAD of *T. complicata* to define the top of the *T. complicata/T. vulnifica* Concurrent Range Zone (see **Biostratigraphy and paleontology** in the Expedition 374 methods chapter [McKay et al., 2019a]). This zone is identified to the base of Site U1525 in Sample 374-U1525A-33X-CC (208.22 m CSF-A), where *T. vulnifica* (whose FAD defines the base of the zone) is still present in the deepest sample examined. *A. fasciculatus* and *A. maccollumi* are also present, leading to the interpretation that the FAD of these taxa were not sampled and that they exist below the interval cored at Site U1525.
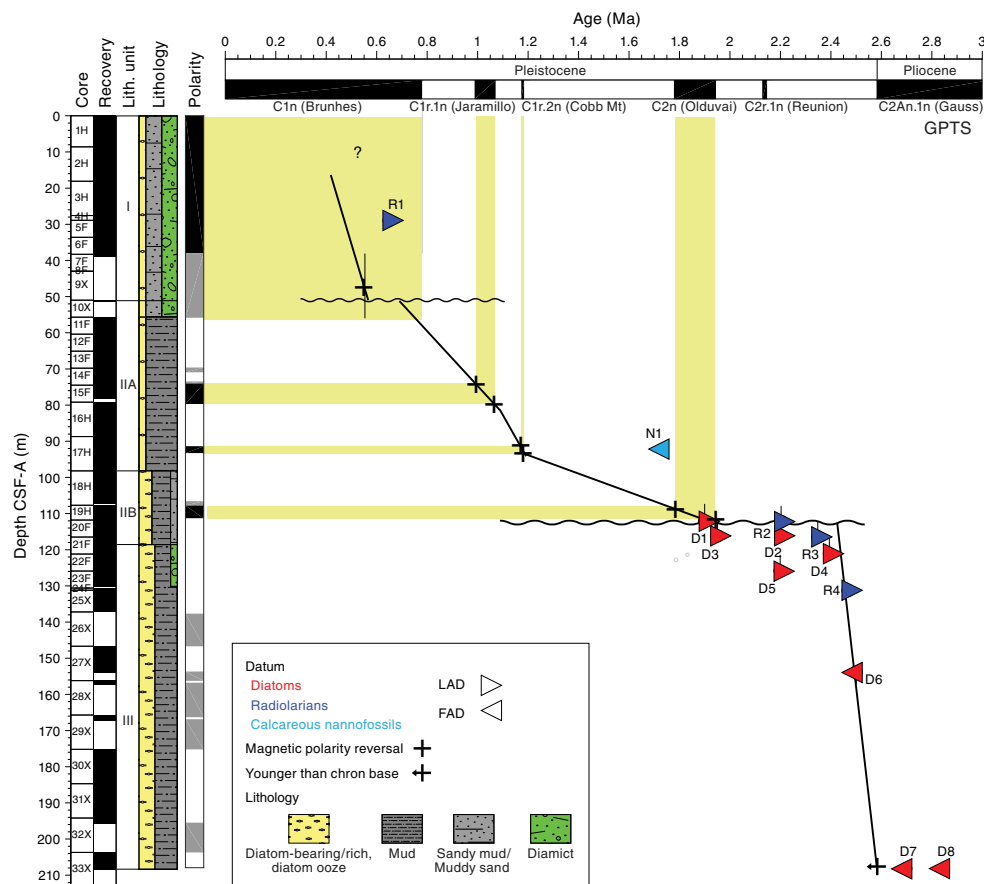

Figure F8. Shipboard age model, Hole U1525A. See Table T5 for biostratigraphic datums and codes. See Paleomagnetism for discussion of paleomagnetic results. Polarity: black = normal, white = reversed, gray = unrecovered or uncertain. Wavy lines = interpreted hiatuses, yellow shading = interpretation of Site U1525 normal polarity results to the geomagnetic polarity timescale of Gradstein et al. (2012).

4.2. Radiolarians

All core catcher samples and the mudline sample from Site U1525 were analyzed for radiolarian content, and a distribution chart is given in Table **T6**. Radiolarians are barren or present in trace abundances and poorly preserved in the uppermost 107.27 m CSF-A (downhole to Sample 374-U1525A-18H-CC). Throughout this interval, only one radiolarian datum is observed, the LAD of *Antarctissa cylindrica* in Sample 4H-CC (28.86 m CSF-A) (Figures **F7**, **F8**, **F9**). Diatom biostratigraphy and seismic evidence suggest extensive mixing of sediments, probably linked to debris flow deposits, over this interval (see **Background and objectives**). This high input of terrigenous material could also cause dilution of radiolarian assemblages, which would explain the very low abundances observed for this group in this part of the section.

The interval from Sample 374-U1525A-19H-CC to Sample 27X-CC (111.84–153.87 m CSF-A) yields moderately to well-preserved radiolarians in frequent to common abundances. Three LADs are observed in this interval: *Cycladophora pliocenica* in Sample 19H-CC (111.84 m CSF-A), *Helotholus vema* in Sample 20F-CC (116.62 m CSF-A), and *Desmospyris spongiosa* in Sample 24F-CC (131.22 m CSF-A) (Figures **F7**, **F8**, **F9**). The high radiolarian abundance (particularly in Sample 27X-CC [153.87 m CSF-A]), together with the abundance patterns of planktonic foraminifers (Figures **F7**, **F9**) and dinoflagellates (also abundant in Sample 27X-CC), seem to suggest deposition in an open-marine environment with reduced influence of sea ice and/or terrigenous input. Disconformities, particularly slow sedimentation rates, and/or sharp changes in environmental conditions occur between Samples 17H-CC and 18H-CC (98.62–107.27 m CSF-A) and between Samples 19H-CC and 20H-CC (111.84–116.62 m CSF-A), where rapid age increases are observed downhole. A strong change in

Table T6. Radiolarian distribution, Hole U1525A. **Download table in CSV format.**
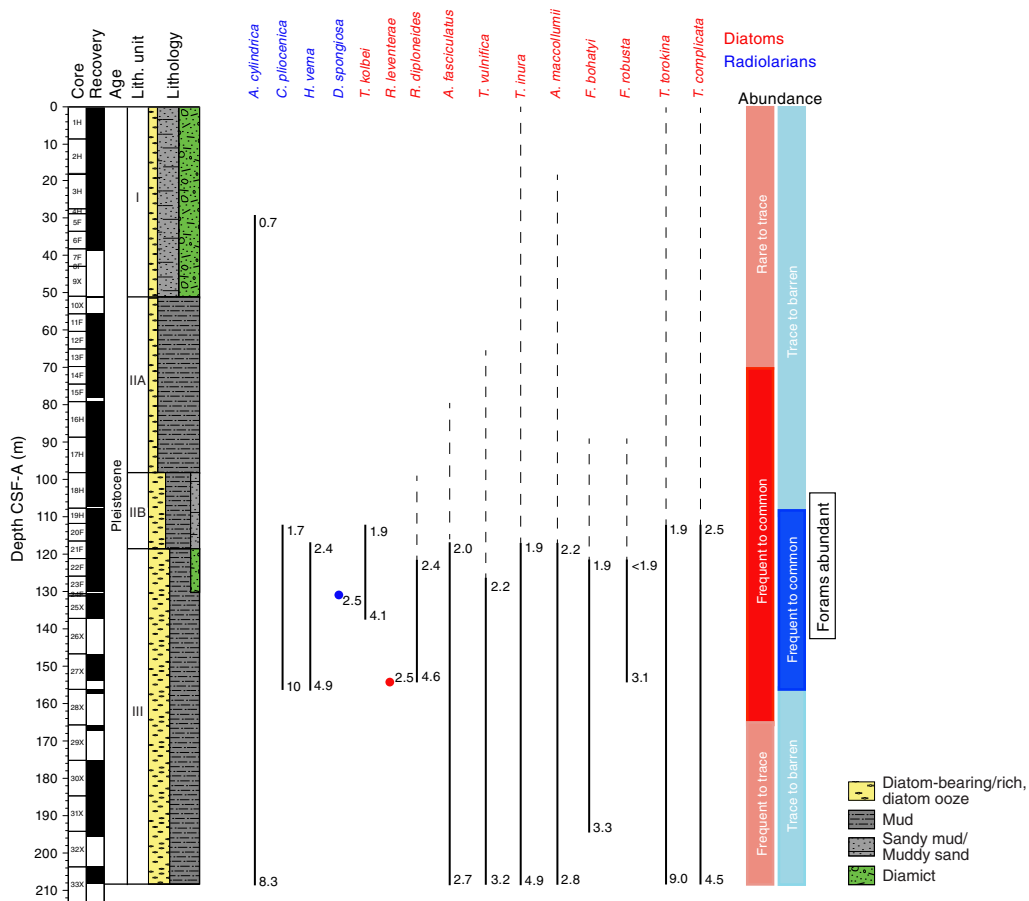

Figure F9. Selected diatom and radiolarian distribution (see Table T4), Hole U1525A. Dashed vertical lines = reworked occurrence. Numbers next to lines indicate FAD and LAD ages in millions of years.

environmental conditions may additionally occur between Samples 27X-CC and 28X-CC (153.87–157.34 m CSF-A), where radiolarian abundances abruptly decrease from common to absent. This decrease makes the observed FAD for *H. vema* in Sample 27X-CC (153.87 m CSF-A) highly questionable, so this datum has not been used to constrain the age model at this site (Table T5 lists the retained diatom and radiolarian datums used to construct the age model in Figure F8). Between Sample 28X-CC (157.34 m CSF-A) and the bottom of the cored sequence (Sample 33X-CC [208.22 m CSF-A]), core catcher samples are barren or contain only trace abundances of radiolarians. Photomicrographs of a few radiolarian species from Sites U1525 and U1524 are shown in Figure F10.
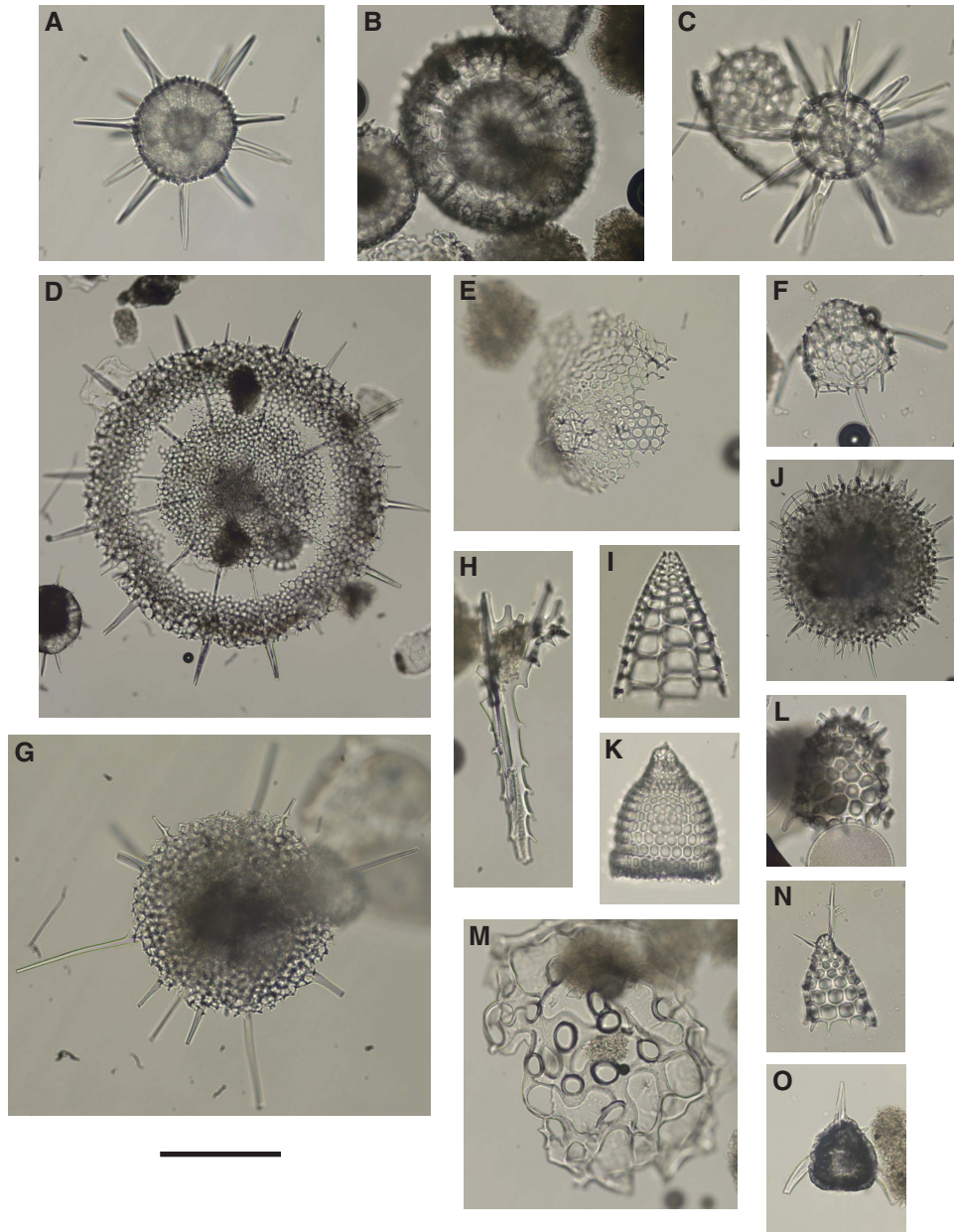

Figure F10. Radiolarians, Sites U1524 and U1525. A. *Actinomma popofskii* (U1525A-1H-1, mudline). B. *Sphaeropyle robusta* (U1524C-8R-CC). C. *Actinomma leptodermum* (U1524A-1H-CC). D, G, J. *Spongotrochus glacialis* (D: U1524A-1H-CC; G, J: U1525A-27X-CC). E. *Velicucullus* sp. cf. *Velicucullus oddgurneri* (U1524C-12R-3, 75–78 cm). F. *Pseudodictyophimus gracilipes* (U1524A-28H-CC). H. *Octodendron* spp. (Keany) spine (U1524A-34X-CC). I. *Peripyramis circumtexta* (U1524A-1H-CC). K. *Cycladophora pliocenica* (U1524C-10R-CC). L. *Ceratocyrtis mashae* (U1525A-27X-CC). M. *Acrosphaera australis* fragment (U1524C-12R-3, 75–78 cm). N. *Cycladophora conica* (U1524C-9R-CC). O. *Pseudodictyophimus planctonis* (U1524C-8R-CC). Scale bar = 100 µm, except D and J = 200 µm.

The primary marker species *Stylatractus universus*, *Pterocanium charybdeum tri-lobum* (both presumably living at much lower latitudes than the Ross Sea area), and *Cycladophora davisiana* (present in the mudline sample and therefore living at this location under modern conditions but absent in core material) are observed in core catcher samples from this site. The marker species *Eucyrtidium calvertense* was only found in the lowermost sample obtained at this site (Sample 374-U1525A-33X-CC [208.22 m CSF-A]), which is dated to >2.47 Ma based on the LAD of *D. spongiosa* in Sample 24F-CC (131.22 m CSF-A). This LAD is much older than the calibrated LAD at ~1.73 Ma (Florindo et al., 2013), which suggests that this event is probably slightly diachronous in different regions of the Southern Ocean and therefore not reliable in the Ross Sea area.

The mudline sample contains a very diverse, modern assemblage made up of 40 species, with significant contributions of *Larcopyle pylomaticus*, *Stylatractus neptunus*, *Actinomma leptodermum*, *Actinomma boreale*, and *Antarctissa denticulata*. The two taxa representative of Antarctic shelf/coastal assemblages (*Rhizoplegma boreale* and the *Phormacantha hystrix*/*Plectacantha oikiskos* group; Nishimura et al., 1997) are either absent or present in negligible numbers, respectively. Many of the species observed in significant numbers (e.g., *A. boreale*/*leptodermum*, *Hexacontium pachydermum*, and *Pseudodictyophimus gracilipes*) are typical components of Arctic/Subarctic assemblages (found in the Greenland Sea close to the summer sea ice edge, the Norwegian Sea, and the Arctic Ocean proper; Swanberg and Eide, 1992; Schröder-Ritzau, 1995; Bjørklund and Kruglikova, 2003). Thus, they may be considered to have a bipolar distribution with equatorial submergence and have probably been advected to the site through the Antarctic Divergence and upwelling of intermediate and deep-water masses. The latter process seems to also be confirmed by the presence of species known to live in intermediate- to deep-water masses (e.g., *Cycladophora davisiana* and *Cornutella profunda*).

Very high abundances of volcanic shards associated with abundant sponge spicules are observed in Sample 374-U1525A-21F-CC (121.05 m CSF-A) and strongly suggest the presence of a cryptic or partially reworked ash layer because a primary ash feature was not observed in the split cores. Such a layer might have been missed or unsampled because of its occurrence in the stratigraphic gaps that occur between cores (see **Depth scales** in the Expedition 374 methods chapter [McKay et al., 2019a]).

4.3. Foraminifers

Foraminifers have variable occurrence and abundance in the Pleistocene section cored at Site U1525 (Table **T7**). In general, the most clay rich samples are foraminifer poor or barren, whereas somewhat sandier mud samples contain planktonic and benthic foraminifers. Mud samples that at first examination appeared to be barren may contain planktonic and/or benthic taxa in the 63–125 µm fraction, which was not routinely examined shipboard. Sand-rich samples are likewise very poor in foraminifers, likely a consequence of dilution by the coarser terrigenous sediments (e.g., Samples 374-U1525A-1H-CC and 33X-CC [8.57 and 208.22 m CSF-A, respectively]) (Figure **F7**).

Sandy mud from Samples 374-U1525A-5F-CC (33.75 m CSF-A) and 7F-CC (38.87 m CSF-A) contains rare (<7) specimens of both planktonic and benthic foraminifers, including sinistrally coiled *Neogloboquadrina pachyderma*, *Globocassidulina subglobosa*, *Angulogerina earlandi*, *Globocassidulina crassa*, *Bulimina aculeata*, and *Cibicides temperatus*; the latter is a yellow-stained, reworked specimen.

A number of the clay-rich samples did not yield any foraminifers during shipboard examination, including Samples 374-U1525A-10X-1, 30–33 cm (51.30 m CSF-A), 12F-CC (65.46 m CSF-A), and 13F-CC (69.73 m CSF-A), whereas other clay-rich samples contain four or fewer specimens (Samples 14F-CC [74.68 m CSF-A], 28X-CC [157.34 m CSF-A]), 30X-CC [184.69 m CSF-A], and 32X-CC [195.84 m CSF-A]. In contrast, several clay-rich samples with small residues of >63 µm fraction material produced small assemblages of foraminifers with relatively numerous specimens (Samples 11F-CC [60.54 m CSF-A], which contains only *N. pachyderma*; 15H-CC to

Table T7. Foraminifer distribution, Hole U1525A.
Download table in CSV format.

20F-CC [78.16–116.62 m CSF-A]; 22F-CC [125.67 m CSF-A]; 23F-CC [130.03 m CSF-A]; and 27F-CC [153.87 m CSF-A]). The most common benthic species in most of these samples are *G. subglobosa* and *Epistominella exigua.* The specimens in some of these samples are very tiny and appear to be size sorted and winnowed by currents. Other specimens, particularly planktonic foraminifer *N. pachyderma*, have holes in chambers, suggesting etching by corrosive deep water. Sample 27X-CC, in contrast, looks more in situ than many samples because of the good preservation and dominance of the agglutinated benthic foraminifer *Miliammina arenacea*, which was found in abundance near the front edge of the Ross Ice Shelf (Osterman and Kellogg, 1979).

A particularly productive foraminifer-rich sandy interval was examined in Sample 374-U1525A-17H-3, 62–64 cm (92.14 m CSF-A). This sample contains abundant planktonic foraminifers (*N. pachyderma*) and nearly 30 species of benthic foraminifers, including *G. subglobosa, A. earlandi, E. exigua, Brizalina* sp. cf. *Brizalina thalmanni, Pullenia bulloides, Pullenia subcarinata, Astrononion antarcticus, Melonis affinis, Gavelinopsis lobatulus, Cibicides refulgens, Cibicidoides* spp., *Fursenkoina fusiformis, Karreriella bradyi,* and numerous species of nodosariids. This diverse, generally well preserved assemblage may represent colonization on a well-oxygenated, winnowed substrate. Alternatively, the broken chambers observed on some of the more delicate taxa suggest that this assemblage, or parts of it, were transported downslope more or less penecontemporaneously. Interestingly, all of the *N. pachyderma* in Sample 17H-3, 62–64 cm, are <250 µm in diameter, suggesting size sorting and winnowing by currents prior to deposition.

In summary, the greatest abundances of foraminifers are found in Samples 374-U1528A-11F-CC to 27X-CC (60.54–153.87 m CSF-A), but the greatest abundances of benthic foraminifers are found in Samples 15H-CC (78.16 m CSF-A) to 27X-CC (Figure **F7**). It is interesting to note that *G. inflata* occurs in Sample 16H-CC (88.86 m CSF-A), whereas *G. bulloides* and *G. falconensis* occur in Sample 22F-CC (125.67 m CSF-A), suggesting episodes of warmer, open, more highly productive surface water (Figure **F11**).
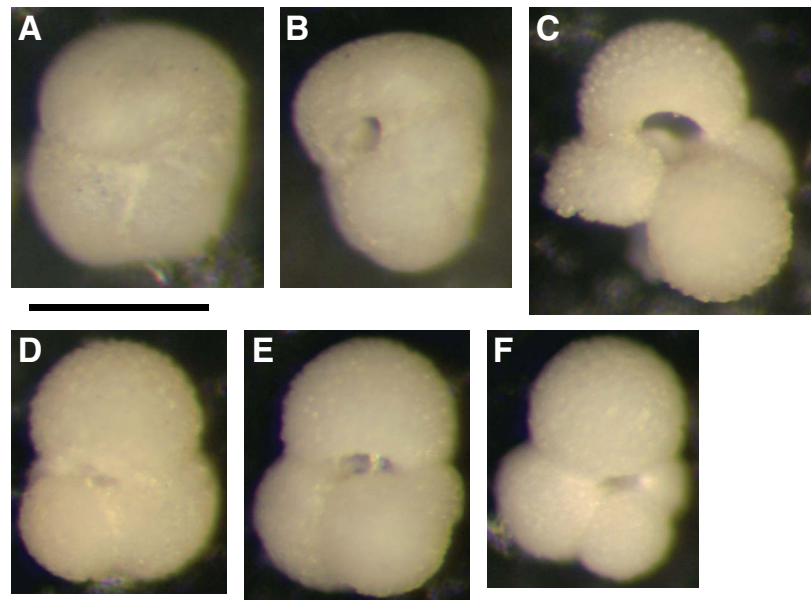

Figure F11. Planktonic foraminifers, Hole U1525A. A, B. *Globoconella inflata* (16H-CC; A: umbilical view; B: edge view). C. *Globigerina bulloides*, broken specimen (22F-CC). D–F. *Globigerina falconensis* (22F-CC). Scale bar = 25 µm.

Table T8. Palynomorph distribution, Hole U1525A. **Download table in CSV format.**

4.4. Palynology

Seven core catcher samples (374-U1525A-20F-CC to 31X-CC [116.62–194.38 m CSF-A]) were analyzed for palynomorph content (Table **T8**) below the interval of reworking identified by siliceous microfossils (Figure **F7**). In general, palynomorphs are moderately to well preserved and absent to rare in Samples 20F-CC (116.62 m CSF-A), 24F-CC (131.22 m CSF-A), 30X-CC (184.69 m CSF-A), and 31X-CC (194.38 m CSF-A); few in Samples 28X-CC (157.34 m CSF-A) and 29X-CC (167.25 m CSF-A); and abundant in Sample 27X-CC (153.87 m CSF-A) (Figure **F7**). The assemblages at Site U1525 are dominated by protoperidinioid dinocysts that are likely cysts of heterotrophic dinoflagellates (mostly *Brigantedinium* spp. and *Selenopemphix* spp.), which are indicative of highly productive water (Zonneveld et al., 2013). Few specimens of the phototrophic *Batiacasphaera* sp. are found. Representative photomicrographs of dinocysts are shown in Figure **F12**.

Sample 374-U1525A-20F-CC (116.62 m CSF-A) is almost devoid of dinocysts; only rare *Brigantedinium* spp. and very rare *Lejeunecysta* sp. are found (Figure **F12**; Table **T8**). The acritarch *Leiosphaeridia* is present in low numbers. Sample 24F-CC (131.22 m CSF-A) is barren of dinocysts, and only the acritarch *Leiosphaeridia* is present in very low numbers.

Sample 374-U1525A-27X-CC (153.87 m CSF-A) exhibits a low diversity dinocyst assemblage of dominant *Brigantedinium* spp., common *Selenopemphix* sp. 1 (Esper and Zonneveld, 2007), few *Selenopemphix antarctica* and *Selenopemphix nephroides*, and rare *Batiacasphaera* spp. The *Brigantedinium* spp. cysts are pigmented light brown, grayish brown, or dark brown and have smooth or granular to scabrate surfaces (Figure **F12**). Some *Brigantedinium* spp. exhibit a paratabulation-like pattern
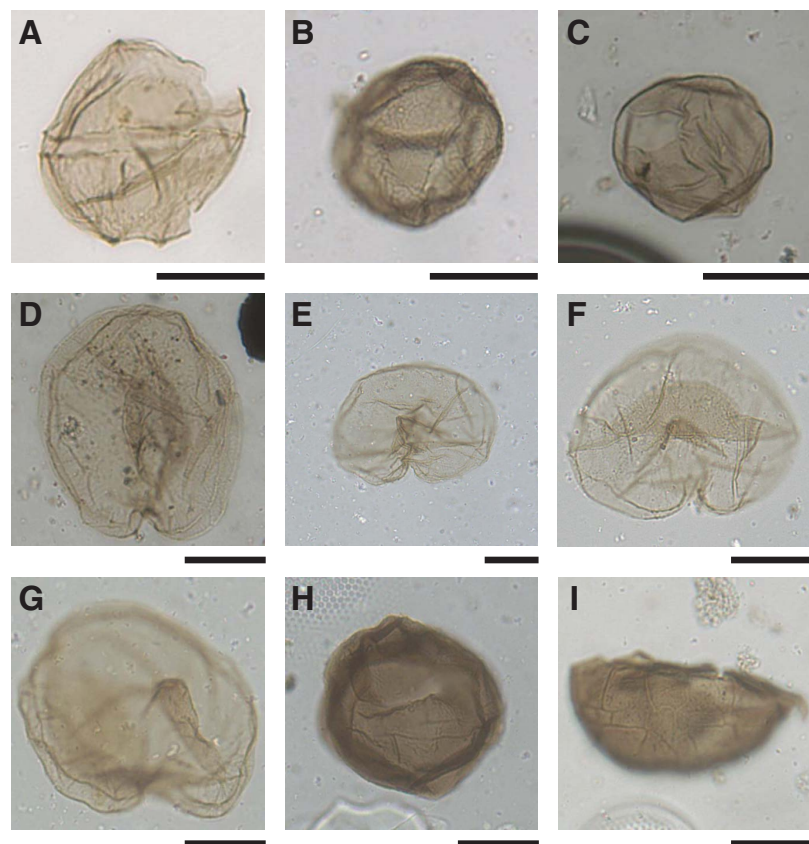

Figure F12. Dinocysts, Hole U1525A. A. *Lejeunecysta* sp. (20F-CC). B, C. *Brigantedinium* sp. (27X-CC; A: textured wall; C: smooth wall). D–G. *Selenopemphix* sp. 1 (27X-CC). H, I. *Brigantedinium* sp., paratabulated (27X-CC). Scale bars = 20 μm.

(Figure **F12**), with features resembling those of the genus *Cryodinium* described from the modern permanent open-ocean zone of the Atlantic Southern Ocean sector (Esper and Zonneveld, 2002); however, the *Brigantedinium* spp. here are generally larger and lack low sutures on a single layered wall. Assemblages composed mainly of *Brigantedinium* spp., *S. antarctica*, and *Selenopemphix* sp. 1 (Figure **F12**) were described from late Quaternary glacial sediments of the Atlantic Southern Ocean (Esper and Zonneveld, 2007) and might reflect productive open-water conditions during the summer season in the Ross Sea.

Samples 374-U1525A-28X-CC (157.34 m CSF-A) and 29X-CC (167.25 m CSF-A) exhibit few *Brigantedinium* spp. and *S. nephroides* and common specimens of the acritarch *Leiosphaeridia*. A few specimens of the transparent *Cymatiosphaera* sp. 1 are found in Sample 29X-CC only. In Samples 30X-CC (184.69 m CSF-A) and 31X-CC (194.38 m CSF-A), rare specimens of *Brigantedinium* spp., *S. nephroides*, and *Batiacasphaera* spp. are found. The acritarch *Leiosphaeridia* is common.

Although palynomorphs are very sparse in the sediments at Site U1525, the dinocyst assemblages point to a high-productivity environment. The low numbers encountered in these samples may be a consequence of high sediment accumulation rates and high input of terrigenous sediments, both of which dilute the biogenic (dinocyst) accumulation. Sample 374-U1525A-27X-CC (153.87 m CSF-A) is remarkable in that it contains abundant and well-preserved dinocysts that are as yet only known from modern circum-Antarctic sediments and open-ocean upper Quaternary Southern Ocean sediments from the Atlantic sector north of the Polar Front (Esper and Zonneveld, 2002, 2007). The occurrence of these dinocysts may imply that the typical recent to modern Southern Ocean dinocyst assemblage first appeared in the Ross Sea in the earliest Pleistocene and that environmental conditions were slightly warmer than at present, with longer seasons of open-water conditions. This aspect merits further postcruise investigation.

4.5. Calcareous nannofossils

Sample 374-U1525A-17H-3A, 82 cm (92.34 m CSF-A), was examined for calcareous nannofossils (Table **T9**). This sample contains a sparse assemblage of moderately preserved Neogene taxa (Figures **F7**, **F13**) that includes *Reticulofenestra minuta*, *Reticulofenestra minutula*, *Calcidsicus leptoporus*, and *Coccolithus pelagicus*. The absence of *Gephyrocapsa* spp. >4 µm is biostratigraphically significant because this group has a FAD at 1.73 Ma. However, additional work needs to be undertaken to support this interpretation because the absence of this group could be due to the sparse nature of the assemblage or the assemblage could be reworked from older sediment.

4.6. Age model

An age model for Site U1525 (Figure **F8**) was developed using a combination of radiolarian and diatom biostratigraphic events (Table **T5**; Figure **F9**) that constrain the age for the lowermost ~100 m of Site U1525 to between 2.4 and 2.6 Ma, with deposition under very high sediment accumulation rates. The entire sequence recovered from Site U1525 is Pleistocene in age based on the age model constructed from biostratigraphic FAD and LAD events (Table **T5**; Figure **F8**) and paleomagnetic reversal events (see **Paleomagnetism**).

Using only those biostratigraphic events that occur below the zone of reworking (deeper than ~100 m CSF-A), a disconformity is identified by the concentration of five diatom and radiolarian LAD events between Samples 374-U1525A-19H-CC and 20F-CC (111.84–116.62 m CSF-A). These five LAD events (D1, D2, D3, R2, and R4 in Figure **F8** and Table **T5**) span from 1.9 to 2.35 Ma, constraining the age of sediments below the disconformity to older than 2.35 Ma and above the disconformity to younger than 1.9 Ma. This younger age control is based on the LAD of *T. kolbei*, a distinctive diatom with a well-documented range indicated as Event D1 in Table **T5** and Figure **F8**. This diatom event provides an important constraint to guide interpretations of magnetic polarity reversals in the interval above this disconformity. The

Table T9. Calcareous nannofossil distribution, Hole U1525A. **Download table in CSV format.**

basal age in the early Pleistocene is supported by the FAD of diatoms *A. fasciculatus* and *A. maccollumii* (FADs at 2.7 and 2.8 Ma, respectively), which are present at the bottom of Site U1525. The age model indicates that the ~96 m thick lithostratigraphic Unit III is an expanded section with a sustained high sediment accumulation rate of >60 cm/ky.

5. Paleomagnetism

Paleomagnetic investigations focused on determining the characteristic remanent magnetization (ChRM) to construct the magnetostratigraphy of Site U1525, which provides chronological constraints when integrated with biostratigraphy. Additionally, a detailed demagnetization sequence was used to investigate the stability and origin of the magnetostratigraphy, and the magnetic fabric was determined to evaluate (post)depositional processes. Measurements of the natural remanent magnetization (NRM) of most archive-half core sections of Cores 374-U1525A-1H through 33X (0–208.27 m CSF-A) were conducted at 5 cm intervals before and after alternating field (AF) demagnetization in 10 mT increments between 0 and 20 mT peak fields.

Core recovery and coring disturbance were dependent on the coring method used. APC and HLAPC cores showed less disturbance and usually very good recovery, whereas XCB cores were more likely to have poorer recovery and drilling disturbance resulting from both the coring process and shattered core liners (see **Operations**). The latter cores are marked as "disturbed," indicating that the orientation of individual core pieces and stratigraphic order is suspect (see **Core disturbance** in the Expedition 374 methods chapter [McKay et al., 2019a]). All cores with substantial drilling disturbance were excluded from the measurement sequence. Occasionally, the disturbance was not easily visible but only apparent in measurement results of the archive-half core sections or in the magnetic fabric data (e.g., parts of Sections 374-U1525A-14F-1 and 15F-1). The data from such intervals were excluded from analysis, as were data
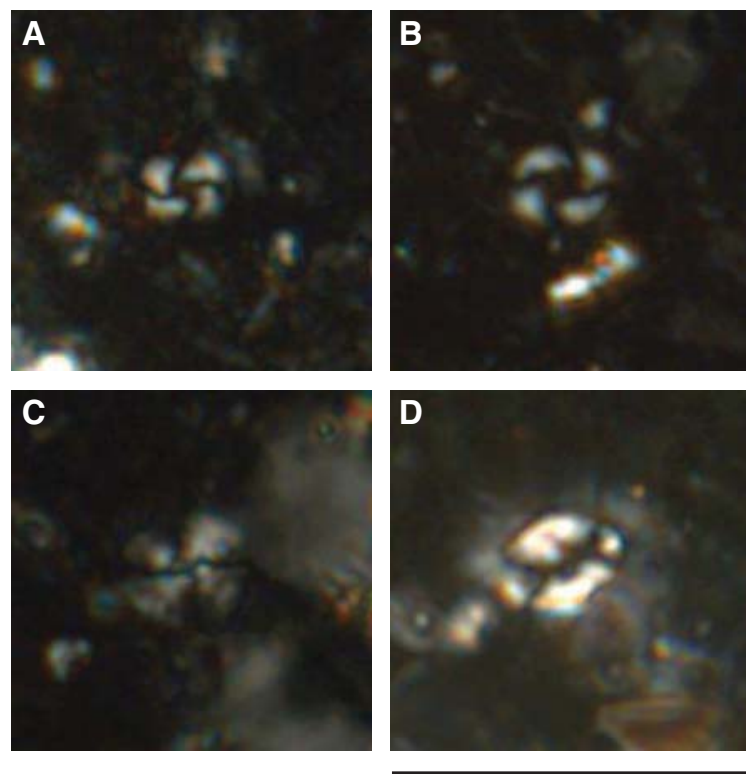

Figure F13. Calcareous nannofossils (U1525A-17H-3A, 82 cm). A. B. *Reticulofenestra minuta*. C. *Calcidiscus leptoporus*. D. *Coccolithus pelagicus*. Scale bar = 10 μm.

collected within 10 cm of section ends because of edge effects. The processed data were used for the construction of the magnetostratigraphy and subsequent correlation to the geomagnetic polarity timescale (GPTS) of Gradstein et al. (2012) using the available independent biostratigraphic age control (see **Biostratigraphy and paleontology**).

A total of 63 oriented discrete paleomagnetic samples (~1–3 per core) were collected to evaluate the coercivity of the magnetic minerals and the quality of the magnetostratigraphy based on measurements of archive-half sections. Seventeen samples were progressively demagnetized using a 20-step AF demagnetization protocol (0–20 mT in 2 mT steps and 20–60 mT in 5 mT steps, followed by 70 and 80 mT peak AF demagnetization) to determine the ChRM, the overprint(s), and their coercivities.

Mean (bulk) magnetic susceptibility and the anisotropy of magnetic susceptibility (AMS) were determined on discrete samples. Mean magnetic susceptibility is compared with magnetic susceptibility measurements made on archive-half core sections using the Section Half Multisensor Logger (SHMSL) and those made on whole-round core sections with the Whole-Round Multisensor Logger (WRMSL). Variability in the AMS data is used to determine magnetic fabric related to variable sedimentary compaction or geological disturbances.

5.1. NRM measurements

5.1.1. Archive-half measurements

Variations in initial NRM intensity correlate well with variations in Kappabridge, WRMSL, and SHMSL magnetic susceptibility, suggesting that magnetic concentration influences these parameters in a similar manner. In contrast, progressive AF demagnetization affects cores from different parts of the stratigraphic succession differently: the NRM intensity of Cores 374-U1525A-2H through 6F and 17H (8.60–38.54 and 88.70–98.67 m CSF-A, respectively) decreases as much as an order of magnitude after 10 mT AF demagnetization (Figure **F14**), whereas the NRM intensity of Cores 11F through 33X (55.70–208.27 m CSF-A), excluding Core 17H, decreases by 30%–50% after demagnetization. Two ~3 m thick intervals of maxima in magnetic susceptibility and initial NRM intensity at ~17 and ~93 m CSF-A (Figure **F14**) coincide with low-coercivity magnetic minerals, which could suggest a (transient) increase in abundance of coarse-grained magnetic material.

NRM inclinations prior to AF demagnetization are steep and positive (Figure **F14**). After progressive AF demagnetization, both positive and negative inclinations occur. The initial positive inclination therefore presumably represents a low-coercivity downward-directed overprint, which is common to IODP coring operations. However, we cannot rule out the possibility that a low-coercivity component unrelated to drilling carries this positive inclination signal. The positive and negative inclinations after 20 mT peak AF demagnetization suggests that these intervals genuinely reflect reversed and normal polarity zones, respectively, because this site is located in the Southern Hemisphere. Inclination should cluster around ±82.4° (the present-day latitude of Site U1525 is 75.0°S) if a geocentric axial dipole is assumed. However, most negative inclinations are somewhat shallower than expected, whereas most positive inclinations are steep (Figure **F14**). The shallowing of negative inclinations may relate to a variety of factors, including (1) depositional processes that are not conducive to recording a primary magnetization, (2) relatively large magnetic grain sizes and associated low magnetic coercivities that make the sediments very susceptible to secondary remagnetization, and (3) drilling overprints that are not completely removed by demagnetization at 20 mT peak AF.

5.1.2. Discrete sample measurements

Results from the oriented discrete samples indicate that a peak AF of 10–16 mT is generally enough to remove a low-coercivity component (Figure **F15**) that may carry as much as 90% of the initial NRM (Figure **F15C**). Further AF demagnetization reveals an intermediate- to high-coercivity (~16–80 mT) ChRM component, which

we interpret to be a primary depositional magnetization. For the normal polarity samples, the demagnetization paths on Zijderveld diagrams do not go directly toward the origin (Figure F15A, F15C). Instead, they overshoot the origin and become noisy. This could result from the existence of a high-coercivity secondary magnetization of unknown origin.

5.2. Magnetostratigraphy

We define two major normal polarity zones (N1 and N2) and three major reversed polarity zones (R1–R3) that are further divided into subzones (e.g., N2.1 and R2.1) (Figure F14). The definition of these zones and subzones primarily depends on core recovery. For example, because there is no core recovery in Core 374-U1525A-26X, we chose to separate Zone R1 from Zone R2 rather than identifying only one zone of reversed polarity with many subzones. Cores 1H through 6F (0–38.54 m CSF-A) have normal polarity and make up Zone N1. The next interval with good recovery, Cores 11F through 25X (55.70–138.16 m CSF-A), has predominantly reversed polarity and is divided into four reversed subzones. Cores 15F, 17H, and 19H (74.50–78.21, 88.70–
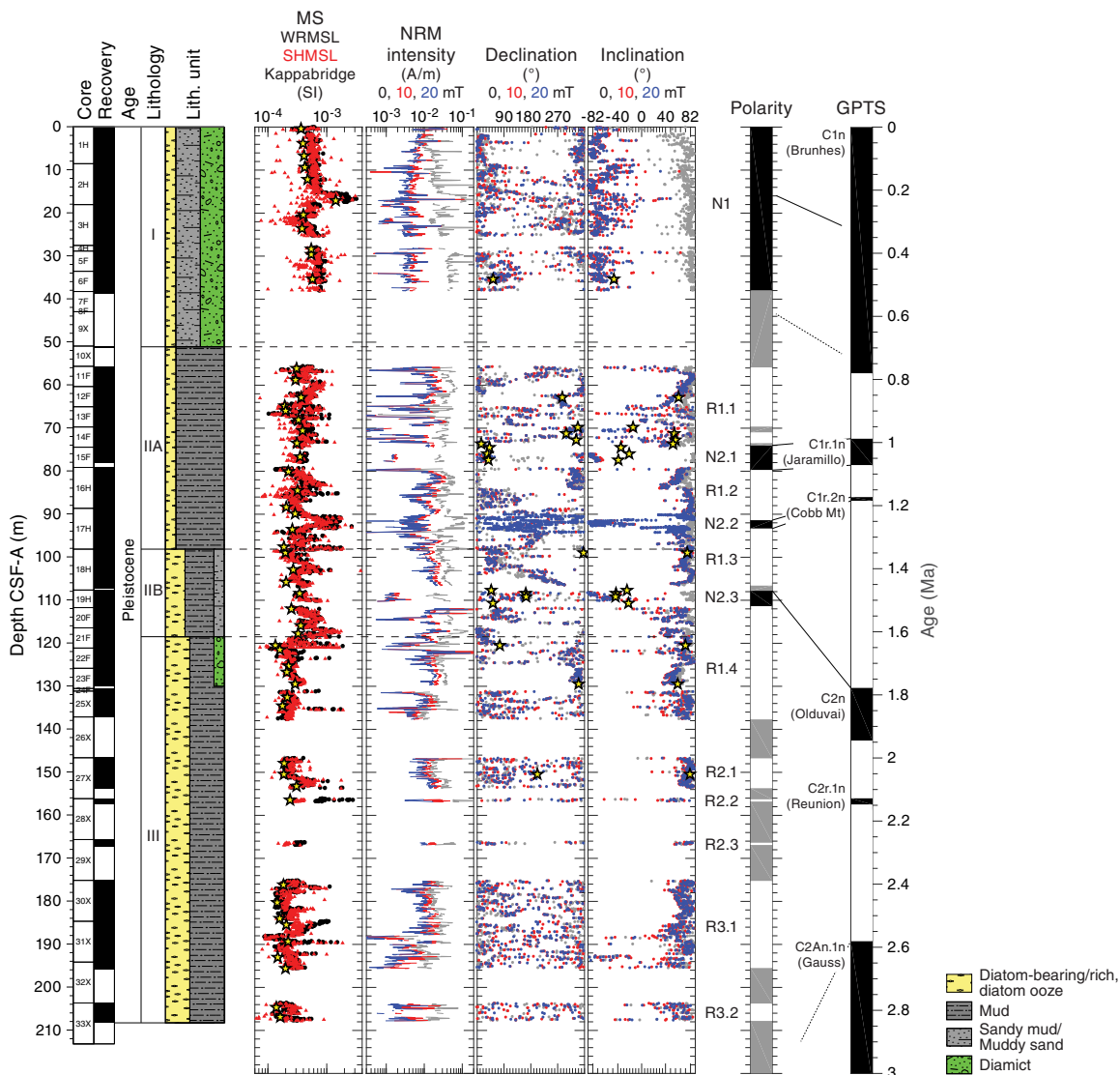

Figure F14. Paleomagnetic data, Hole U1525A. GPTS from Gradstein et al. (2012). MS: black circles = WRMSL, red triangles = SHMSL, yellow stars = Kappabridge. Intensity, declination, and inclination: gray = initial NRM, red = after 10 mT peak AF demagnetization, blue = after 20 mT peak AF demagnetization, yellow stars = discrete samples. Polarity: black = normal (N), white = reversed (R), gray = uncertain or no recovery. Note that Site U1525 is in the Southern Hemisphere, and positive inclination corresponds to a reversed polarity interval. See text for discussion of polarity Zones N1 through Subzone R3.2.

98.67, and 107.70–111.89 m CSF-A, respectively) contain thin intervals of normal polarity that we identify as Subzones N2.1–N2.3. We further identify reversed polarity Zone R2 in Cores 27X through 29X (146.70–167.30 m CSF-A) and Zone R3 in Cores 30X through 33X (175.20–208.27 m CSF-A).
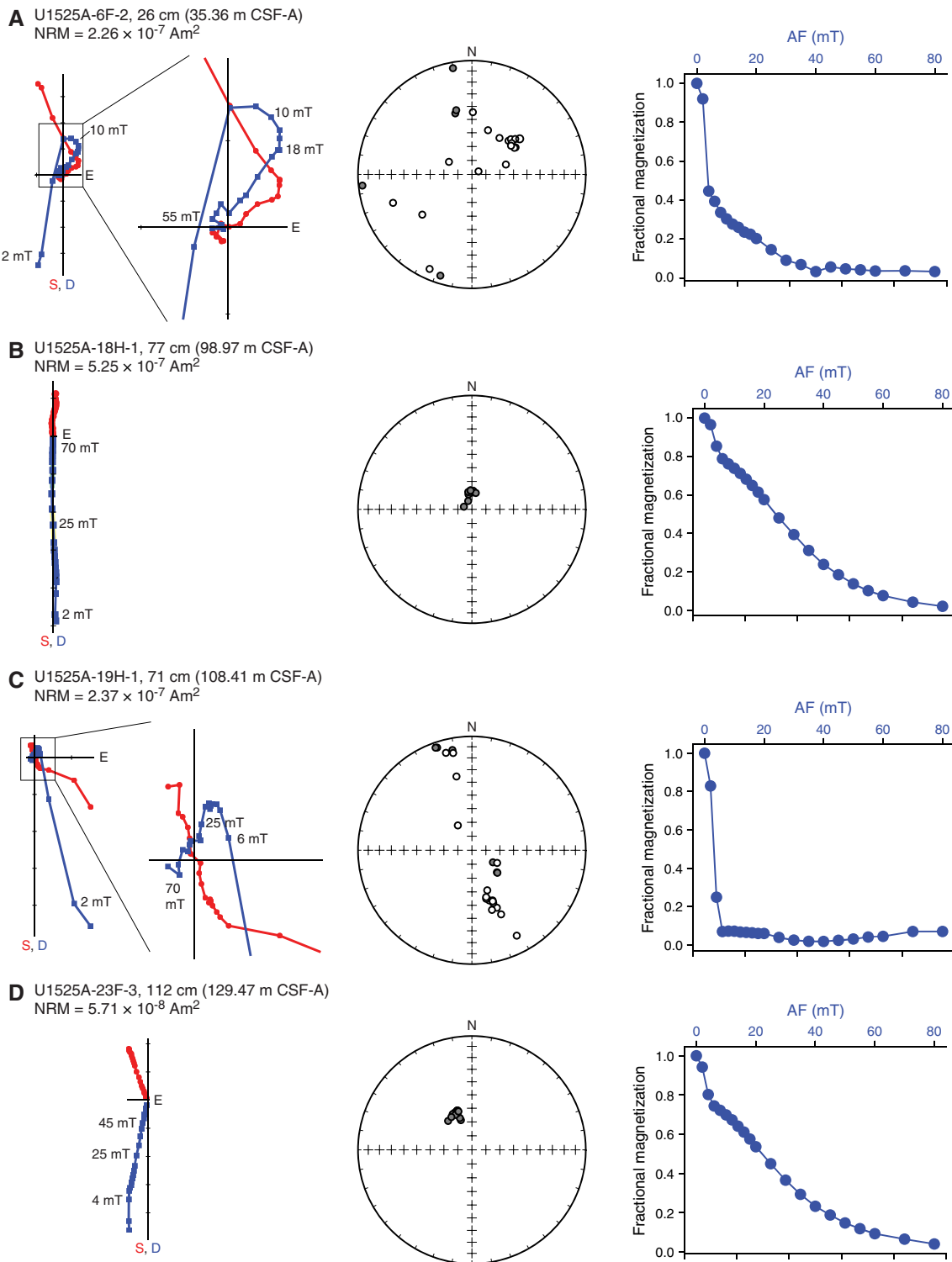

Figure F15. Representative AF demagnetization behavior of oriented discrete samples, Hole U1525A. From left to right for each sample: Zijderveld diagrams with peak AF fields and initial NRM, equal area projections of directions during demagnetization (gray solid circles = lower hemisphere, open circles = upper hemisphere), and fractional magnetization (normalized to initial NRM) during AF demagnetization. A, C. Samples from normal polarity zone. B, D. Samples from reversed polarity zone.

The correlation of these polarity zones to the GPTS of Gradstein et al. (2012) requires independent biostratigraphic age control (see **Biostratigraphy and paleontology**). Biostratigraphy indicates that the upper ~90 m CSF-A contains significant proportions of reworked species and is therefore difficult to date. An angular unconformity at ~50 m CSF-A is inferred from seismic records and lithologic features, suggesting a stratigraphic break at this level (indicated as an unconformity on the preliminary age-depth model in Figure **F8**; see **Background and objectives** and **Lithostratigraphy**). Because core recovery is very good in the upper ~39 m CSF-A and the mudline sample contains an extant radiolarian fauna, we assume that Zone N1 is relatively continuous and can be tied fully to the Brunhes Chron (0–0.781 Ma) (Figure **F14**).

Excellent biostratigraphic tie points are available for Cores 374-U1525A-19H through 33X, and they indicate a latest Pliocene to earliest Pleistocene age (see **Biostratigraphy and paleontology**) (Figure **F14**; Table **T10**). We therefore tie reversed polarity Zones R2 and R3 to Subchron C2r.2r (2.148–2.581 Ma). The absence of a normal polarity zone implies that the lowermost cores at Site U1525 are of Pleistocene age. In addition, these biostratigraphic tie points imply a short hiatus between Cores 19H and 20F and provide an age of younger than ~1.9 Ma for Core 19H. The ages of normal polarity Subzones N2.1, N2.2, and N2.3 are therefore younger than 1.9 Ma, and we tie these to the Jaramillo Subchron (0.988–1.072 Ma), Cobb Mountain Subchron (1.173–1.185 Ma), and Olduvai Chron (1.778–1.945 Ma), respectively (Figure **F14**; Table **T10**).

5.3. Magnetic susceptibility and AMS

We measured the mean magnetic susceptibility and AMS tensor of all collected discrete samples. The orientation and magnitude of the maximum (k_{max}), intermediate (k_{int}), and minimum (k_{min}) axes determines the shape of this AMS tensor. The degree of anisotropy (P) of each tensor is approximated by the k_{max}/k_{min} ratio, where $P = 1$ indicates no anisotropy (spherical shape) and $P > 1$ indicates a high degree of anisotropy (Figure **F16**). We observed a downhole increase toward higher P values (from ~1.1 in the upper 35 m CSF-A to ~1.2 at ~190 m CSF-A) (Figure **F16**).

When P is >1 (i.e., anisotropic sample) and k_{min} inclination is >60° (i.e., minimum susceptibility axis is steep), compaction most likely causes the anisotropy. This compaction is common in sedimentary settings represented by the sediment deposited in lithostratigraphic Units II and III. The shallow k_{min} inclinations observed in Cores 374-U1525A-13F through 15F, 17H, 19H, and 20F may be related to subtle disturbances induced by either drilling or geological processes (e.g., turbidites). In Unit I, relatively subdued P values and scattered k_{min} inclinations indicate that these sediments are not compacted in the same way as those in Units II and III. This distinction correlates well with the sedimentary differences in lithostratigraphic units; the major lithologies of Unit I are sandy mud and muddy diamict, whereas Units II and III are predominantly mud-rich and diatom-bearing/rich lithologies.

Table T10. Preliminary magnetostratigraphic tie points, Hole U1525A. **Download table in CSV format.**

Chron boundary	Age (Ma)	Top core, section, interval (cm)	Depth CSF-A (m)	Bottom core, section, interval (cm)	Depth CSF-A (m)	Midpoint depth CSF-A (m)	Comments
		374-U1525A-		374-U1525A-			
C1r.1r/C1r.1n	0.988	14H-4, 85	73.66	15H-1, 90	75.40	74.530	Core gap
C1r.1n/C1r.2r	1.072	15H-3, 40	77.62	16H-1, 0	79.20	78.410	Core gap
C1r.2r/C1r.2n	1.173	17H-2, 126	91.37	17H-3, 22	91.74	91.555	
C1r.2n/C1r.3r	1.185	17H-3, 132	92.84	17H-4, 11	93.04	92.940	
C1r.3r/C2n	1.778	19H-1, 20	107.90	19H-1, 55	108.25	108.075	

6. Physical properties

Physical property measurements were completed on whole-round sections, section halves, and discrete samples from Site U1525. Some outliers and unreliable values were excluded from the plotted data (Table **T11**). Following thermal equilibration (~4 h), gamma ray attenuation (GRA) bulk density, magnetic susceptibility, *P*-wave velocity (*P*-wave logger [PWL]; on APC and HLAPC cores only), and natural gamma radiation (NGR) measurements were made on all whole-round sections using the WRMSL and Natural Gamma Radiation Logger (NGRL). Sampling resolution for the WRMSL was 2.5 cm, and NGR was measured at 10 cm intervals. Thermal conductivity measurements were conducted using the full-space needle probe for APC and HLAPC cores, typically on Sections 2 and 5.

Discrete samples from the working-half sections (typically from Sections 1, 3, 5, and 7) were taken for moisture and density (MAD) measurements for generating bulk and grain density and porosity data. Shear strength measurements were also taken on every other working-half section of APC and HLAPC cores using the Torvane shear device. Discrete compressional (*P*-wave) velocity measurements were conducted on the working-half sections of each core section using the *P*-wave caliper (PWC) contact probe system on the Section Half Measurement Gantry (SHMG). Color reflectance and point magnetic susceptibility data were collected on archive-half sections
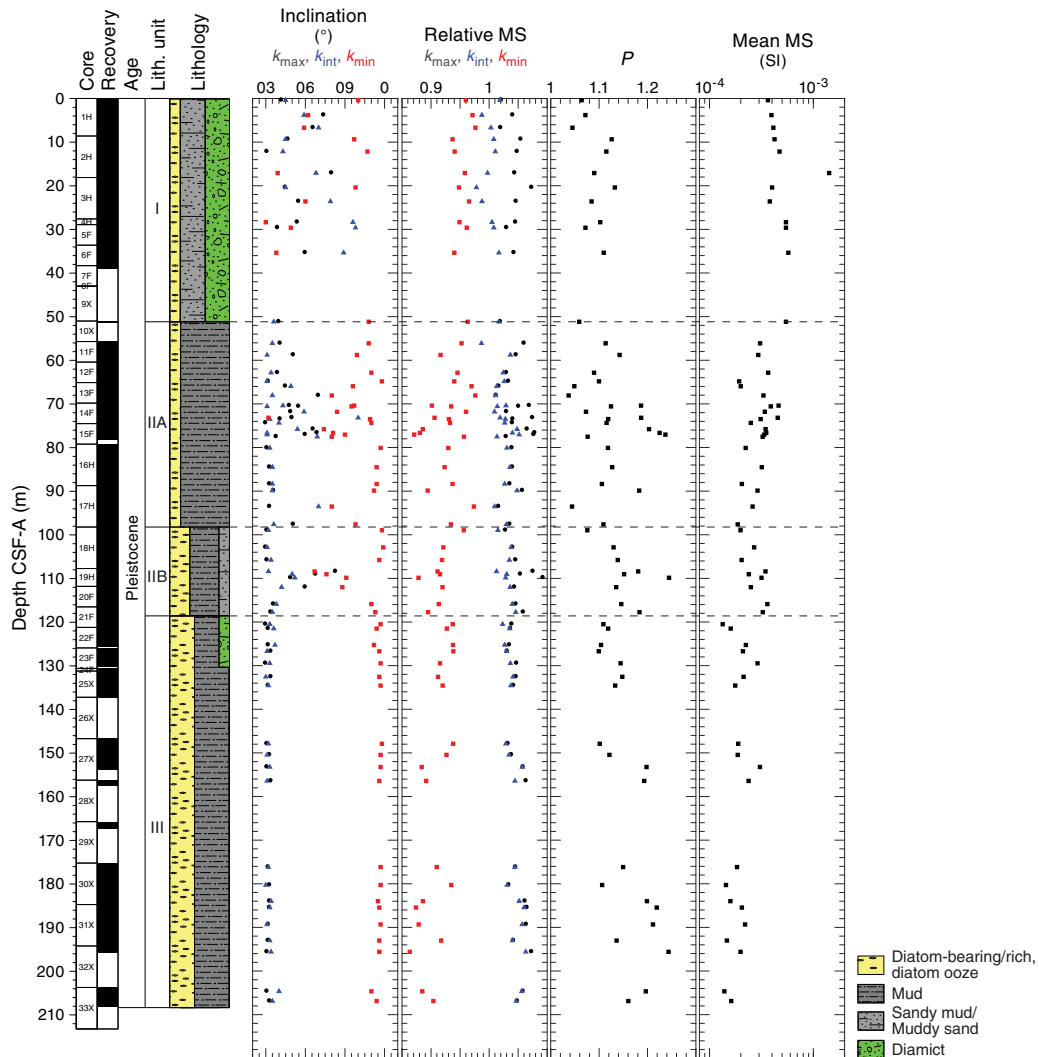

Figure F16. Anisotropy of magnetic susceptibility, Hole U1525A. Degree of anisotropy (*P*) is approximated by the k_{max}/k_{min} ratio, in which *P* = 1 indicates no anisotropy and *P* > 1 is more anisotropic. Mean magnetic susceptibility is the average of k_{max}, k_{int}, and k_{min}.

using the SHMSL. Red, green, and blue (RGB) were measured on the Section Half Imaging Logger (SHIL) (see **Lithostratigraphy** and **Physical properties** in the Expedition 374 methods chapter [McKay et al., 2019a]).

The physical property measurements are in good overall agreement with the defined lithostratigraphic units. In particular, a downhole increase in magnetic susceptibility and NGR in lithostratigraphic Unit I corresponds to lithologic variation in diatom-bearing sandy mud and muddy diamict. Fluctuating magnetic susceptibility and NGR values in Unit II correlate to interbedded intervals of diatom-bearing/rich mud and sandy mud. Relatively low magnetic susceptibility, NGR, and bulk and grain densities in Unit III are characteristic of diatom ooze and diatom-rich mud and sandy mud. Whole-round measurements on XCB cores often underestimate values for measurements that rely on volume (e.g., bulk density) because XCB cores do not completely fill the core liner. Therefore, the depth at which XCB coring initiated is shown on all figures for reference. Note that Cores 374-U1525A-9X and 10X were collected in the upper part of the hole, but core recovery was minimal, so these data are not specifically designated as being cored with the XCB coring system (see **Operations**). All physical property data are available from the Laboratory Information Management System (LIMS) database (**http://web.iodp.tamu.edu/LORE**).

6.1. Magnetic susceptibility

Whole-round measurements on the WRMSL and discrete point measurements on the SHMSL were used to characterize magnetic susceptibility at Site U1525 (Figure **F17**). Both methods yield similar downhole variability and a similar range of values from ~0 × 10^{-5} to ~330 × 10^{-5} SI. Low magnetic susceptibility values in the WRMSL data correspond to mud or clast-poor muddy diamict (e.g., Sections 374-U1525A-3H-3 and 16H-1). Poor recovery limited WRMSL measurements in several intervals of the hole, especially in Cores 7F through 10X (38.3–51.33 m CSF-A). Magnetic susceptibility in lithostratigraphic Unit I varies from ~30 × 10^{-5} to ~85 × 10^{-5} SI. Magnetic susceptibility increases slightly with depth, except in parts of Cores 2H and 3H. The exceptionally high peaks in Cores 2H and 3H (>200 × 10^{-5} SI) likely reflect the increase in abundance of individual clasts in this interval. In Unit II (51.11–118.58 m CSF-A), magnetic susceptibility varies downhole, predominantly between 20 × 10^{-5} and ~60 × 10^{-5} SI, and appears cyclic. These cyclic changes may reflect changes in composition of diatom-bearing mud and/or changes in clast composition. In Unit III, magnetic susceptibility is relatively low but varies from ~20 × 10^{-5} to ~40 × 10^{-5} SI. Lower average magnetic susceptibility values likely reflect an increased presence of diatom ooze and diatom-rich mud. In addition, incompletely filled XCB Cores 25X

Table T11. Physical property data exclusion schema, Site U1525. LIMS = Laboratory Information Management System. WRMSL = Whole-Round Multisensor Logger, SHMSL = Section Half Multisensor Logger, GRA = gamma ray attenuation, NGRL = Natural Gamma Radiation Logger, PWC = *P*-wave caliper, MAD = moisture and density. NA = not applicable. **Download table in CSV format.**

Measurement	Instrument	LIMS edge trim (cm)	Excluded values	Data points excluded (%)
Magnetic susceptibility	WRMSL	12	>200 10^5 SI	1.1
Magnetic susceptibility	SHMSL	12	>200 10^5 SI	0.3
GRA bulk density	WRMSL	12	<1.2 and >2.6 g/cm^3	0.7
Natural gamma radiation	NGRL	12	NA	NA
P-wave	WRMSL	12	<1400 and >2600 m/s	0.6
P-wave	PWC	NA	<1400 and >2600 m/s	1.8
Thermal conductivity	TK04	NA	Manually	3
MAD bulk density	MAD	NA	<1.2 and >2.6 g/cm^3	1.6
MAD porosity	MAD	NA	<20% and >70%	1.6
MAD grain density	MAD	NA	<2.4 and >2.6 g/cm^3	1.6
Shear strength	Torvane	NA	NA	NA
Color	SHMSL	NA	NA	NA

through 33X (131.2–208.27 m CSF-A) may cause lower magnetic susceptibility values compared with Units I and II.

6.2. Natural gamma radiation

NGR varies between ~33 and 68 counts/s (Figure F17). NGR in lithostratigraphic Unit I (e.g., Cores 374-U1525A-1H through 10X [0.0–55.70 m CSF-A]) slightly increases downhole from ~40 to 58 counts/s, with a peak (~68 counts/s) in Sections 2H-5 and 2H-6. The peak correlates with high magnetic susceptibility and corresponds to diatom-bearing clast-rich muddy diamict. In Unit II (51.11–118.58 m CSF-A), NGR shows a downhole cyclic trend similar to magnetic susceptibility, varying between ~50 and 62 counts/s with ~6–12 m apparent cyclicity. These repetitions may reflect interbedded diatom-bearing to diatom-rich mud and/or sandy mud in Unit II. In general, NGR decreases downhole in Subunit IIA, whereas it increases downhole in Subunit IIB. NGR in the upper part of Unit III (Cores 22F through 24F [121.2–131.28 m CSF-A]) slightly decreases from ~50 to 45 counts/s, corresponding to diatom-rich mud. Overall, low values (33–46 counts/s) measured on the XCB cores (25X through 33X [131.2–208.27 m CSF-A]) are consistent with the presence of diatom ooze and diatom-rich mud and also are likely affected by incompletely filled core liners.

6.3. Bulk density, grain density, and porosity

Discrete MAD samples yielded bulk density values concentrated in a narrower range (~1.6–2.2 g/cm³) relative to GRA bulk density measurements (~1.0–2.6 g/cm³) (Figure F18). For APC and HLAPC cores (374-U1525A-1H through 24F [0–131 m CSF-A]), density measurements from discrete samples are generally lower than GRA bulk density measurements, whereas for XCB cores, it is the opposite. Furthermore,
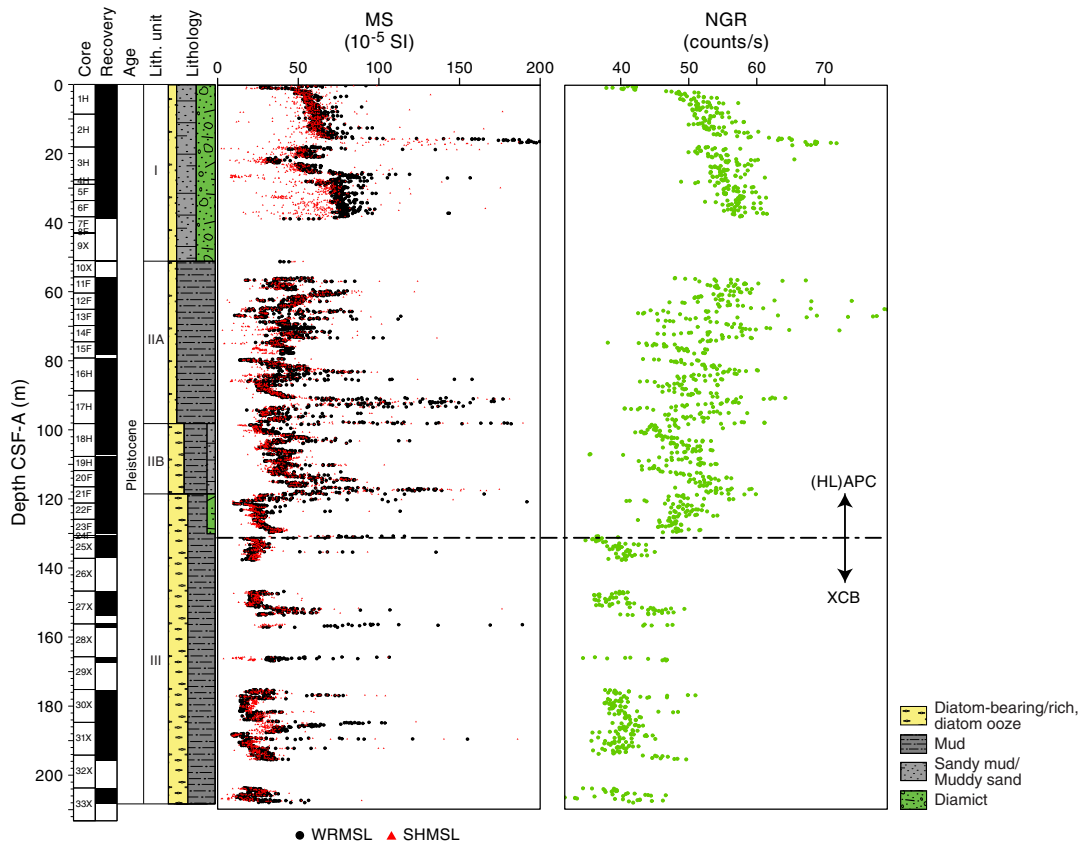

Figure F17. MS and NGR, Hole U1525A.

discrete-sample bulk density above and below the transition from APC/HLAPC to XCB coring remains unchanged, whereas whole-round density measurements decrease at the transition, likely because XCB cores do not completely fill the core liner and are usually more disturbed than APC/HLAPC cores.

In lithostratigraphic Unit I, bulk density generally increases downhole, with peak density in Sections 374-U1525A-2H-5 and 2H-6 (~14.6–17.6 m CSF-A) corresponding to peaks in magnetic susceptibility and NGR that are related to clast-rich muddy diamict. Porosity decreases downhole in the upper ~40 m CSF-A, suggesting that compaction and/or lithology are controlling downhole variation in these properties. Grain density also decreases downhole through Unit I, indicating a change in lithologic composition or grain size. In Unit II, bulk density is lower relative to Unit I and is consistently ~1.7 g/cm³. Grain density is relatively low compared with Unit I, whereas porosity is relatively high. In Unit III, bulk density and grain density increase slightly from Section 27X-3 through Section 28X-1 (~152–157 m CSF-A), whereas porosity decreases, associated with increased clast abundance in this interval. Throughout the lower parts of Unit III, bulk density is ~1.7 g/cm³, and together with porosity does not significantly vary downhole, with values similar to Unit II, whereas grain density decreases downhole slightly. Overall, bulk and grain densities are the lowest in Unit III, reflecting increased diatom content.

6.4. Compressional *P*-wave velocity

P-wave velocity measurements range from ~1500 to 2800 m/s on the PWL and from ~1500 to 1900 m/s on the PWC and overall are in good agreement on the low end (Figure **F19**). PWL measurements were discontinued at Core 374-U1525A-25X (131 m CSF-A) because of the switch from HLAPC coring to XCB coring. In lithostratigraphic Unit I, *P*-wave velocity increases downhole from 1600 to 1800 m/s, which is consistent with compaction. A maximum *P*-wave velocity of ~2000 m/s occurs in Sections 2H-5 and 2H-6 (14.6–17.6 m CSF-A) and is related to a clast-rich diamict (see **Lithostratigraphy**). In Unit II, *P*-wave velocity from the PWC remains constant at ~1600 m/s and is relatively low compared with the overlying unit, likely
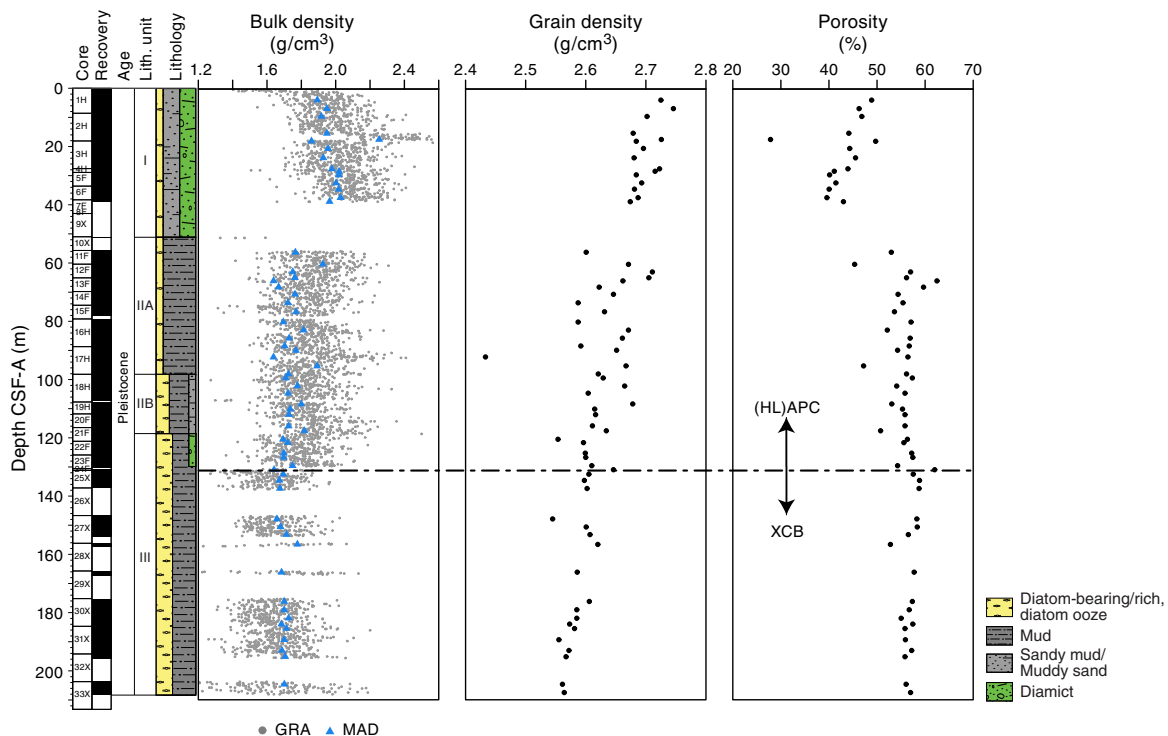

Figure F18. GRA and MAD bulk density, grain density, and porosity, Hole U1525A.

because of increased abundance of diatoms in mud-dominated lithologies. A small decrease in velocity from 1600 to 1550 m/s occurs at the boundary between Units II and III, reflecting increased abundance of diatoms in Unit III. Slightly increased *P*-wave velocity in Section 28X-1 reflects an increased abundance of clasts in this section.

6.5. Shear strength

Shear strength measurements vary from 0.1 to 9.5 kg/cm² (Figure **F19**). In lithostratigraphic Unit I, shear strength increases with depth from 0.1 to 5.6 kg/cm², likely because of compaction and decreasing moisture content with depth. A short interval (Sections 374-U1525A-2H-5 and 2H-6) has very high values (~8 kg/cm²) that correspond to a clast-rich muddy diamict also detected in other physical property measurements. In Unit II, shear strength increases from 2 to 6 kg/cm², likely because of increased compaction with depth. We note that the increase in this lower part of the hole is more gradual compared with the upper part of the hole, which might be explained by differing sedimentation rates between the two units and/or by different accumulation processes (event-bed dominated versus hemipelagic dominated). Low values (<2 kg/cm²) observed in Section 14H-1 correspond to sandy mud, with shear strength increasing from bottom to top. However, low shear strength observed in Cores 15H and 19H most likely reflects coring disturbance rather than lithologic change. In the upper part of Unit III, shear strength increases downhole from 5 to 10 kg/cm², perhaps because of compaction. The cores below Core 30X were not measured because they are lithified.

6.6. Thermal conductivity

The quality of thermal conductivity measurements from APC and HLAPC cores was checked by evaluating two parameters: (1) the number of solutions acquired and (2) the shape of the curve formed on the temperature versus time plot of these points. A valid measurement must have a sufficient number of solutions to form an exponen-
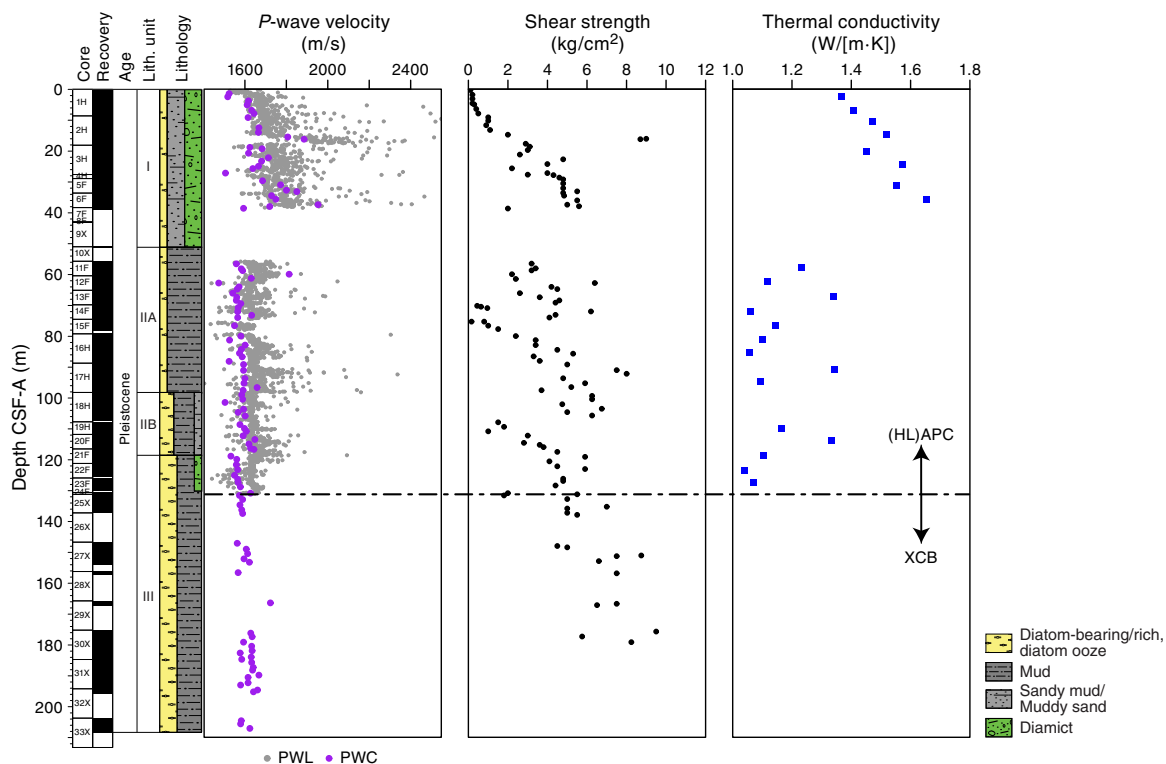

Figure F19. *P*-wave velocity, shear strength, and thermal conductivity, Hole U1525A.

tial curve. All measurements with a low number of solutions and/or a bad repartition of these values on the temperature versus time plot (i.e., forming two curves or no curve) were deleted, resulting in removal of 3% of the original data. In lithostratigraphic Unit I, thermal conductivity increases downhole from 1.4 to 1.7 W/(m·K) (Figure **F19**). In Unit II, thermal conductivity is generally lower than in Unit I, with measurements between 1.0 and 1.4 W/(m·K) and no systematic downhole trend. Thermal conductivity measurements were not carried out below Core 374-1525A-25X (131 m CSF-A) because of the switch to XCB coring in more lithified sediment.

6.7. Color reflectance spectroscopy

Color reflectance spectroscopy data were acquired on section halves using the SHMSL (Figure **F20**). In lithostratigraphic Unit I, L* and b* decrease, whereas a* increases downhole, suggesting that the sediment darkens and both yellow and green colors decrease with depth. In Subunit IIA, L* and a* increase slightly downhole, whereas b* remains unchanged, which indicates that the sediment becomes lighter and less green downhole. Relative to Unit I, a* is much lower, indicating that Subunit IIA is greener than Unit I, possibly reflecting increased diatom content. In Subunit IIB and the upper part of Unit III shallower than 131 m CSF-A, L* decreases slightly downhole and a* remains similar. In the lower part of Unit III, deeper than 131 m CSF-A, L* is lower overall but increases with depth, indicating downhole lightening of sediment. In this unit, a* remains unchanged and b* increases and then decreases toward the bottom of the hole, indicating increasing and then decreasing yellow color of the sediment.

6.8. Summary

In general, data from whole-round measurements are in good agreement with those from split-core measurements (Figure **F21**). Downhole changes in physical properties
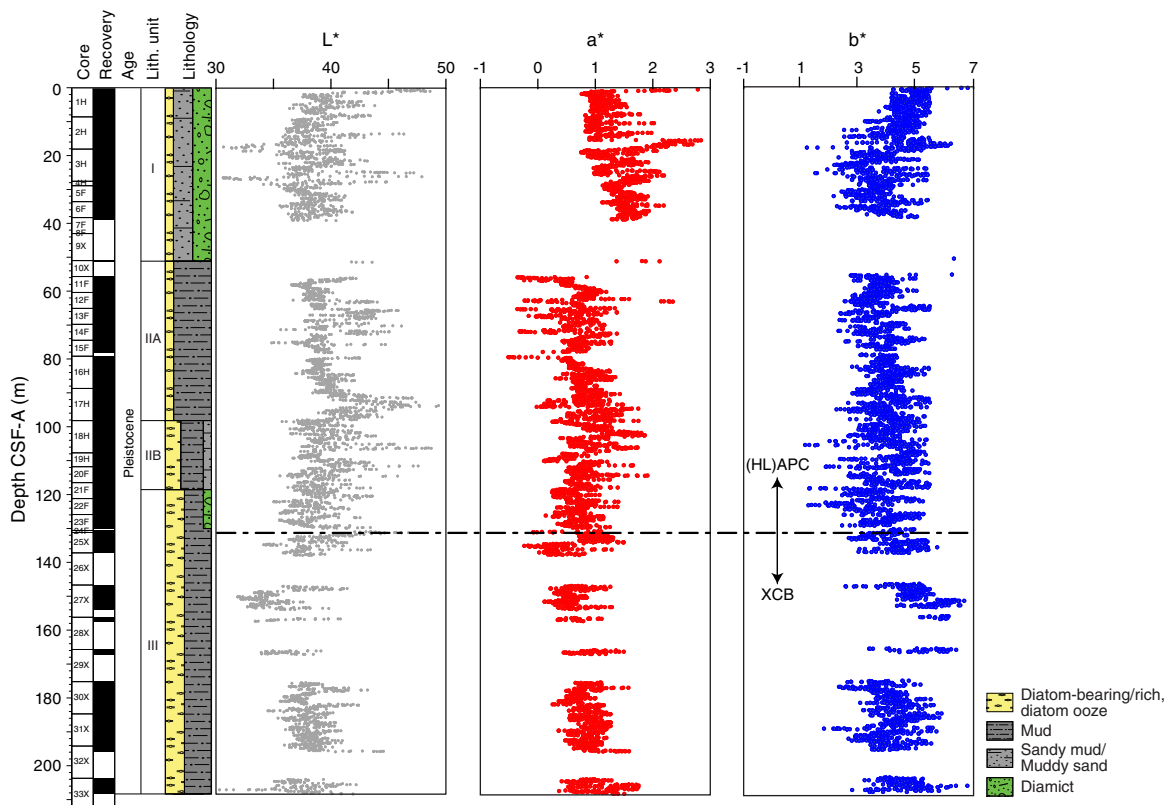

Figure F20. Color reflectance spectroscopy, Hole U1525A.

are in good overall agreement with the defined lithostratigraphic units based on sedimentological characteristics (see **Lithostratigraphy**; Figure **F21**; Table **T12**), and changes in physical properties provide insight into lithologic changes in and seismic-reflection expression of (Figure **F22**) the units. Because of the lack of downhole sonic measurements, we relied on core-based *P*-wave measurements for depth-converting the lithostratigraphic and physical properties units and to correlate them with the seismic-reflection profile crossing Site U1525.

Lithostratigraphic Unit I records a downhole increase in magnetic susceptibility, NGR, density, *P*-wave velocity, and shear strength and a decrease in porosity. These changes reflect both compaction and changes in lithology in this unit of diatom-bearing sandy mud interbedded with clast-poor muddy diamict. In Unit I, Sections 374-U1525A-2H-5 and 2H-6 contain peaks in magnetic susceptibility, NGR, density, *P*-wave velocity, and shear strength and decreased porosity that reflect increased clast and clay content and compaction in this clast-rich diamict. In Unit II, multimeter-scale cyclicity apparent in magnetic susceptibility and NGR is likely related to downhole changes in lithology. In Unit II, relatively consistent density, *P*-wave velocity, and porosity indicate minimal changes in lithology in the diatom-bearing/rich mud and sandy mud beds. Shear strength in Unit II also demonstrates downhole changes that may be related to lithologic changes or compaction. Generally lower magnetic susceptibility, NGR, density, and *P*-wave velocity in Unit III reflect increased diatom content.

This unit division is also reflected by the seismic facies (Figure **F22**). Lithostratigraphic Unit I corresponds to a package of high-amplitude, subhorizontal reflectors partly covered by seafloor-ringing reflectors (Figure **F22**). These reflectors represent the top part of a wedge-shaped seismic unit with low-amplitude and discontinuous reflectors that pinches toward the northwest and onlaps on, or laterally interfingers
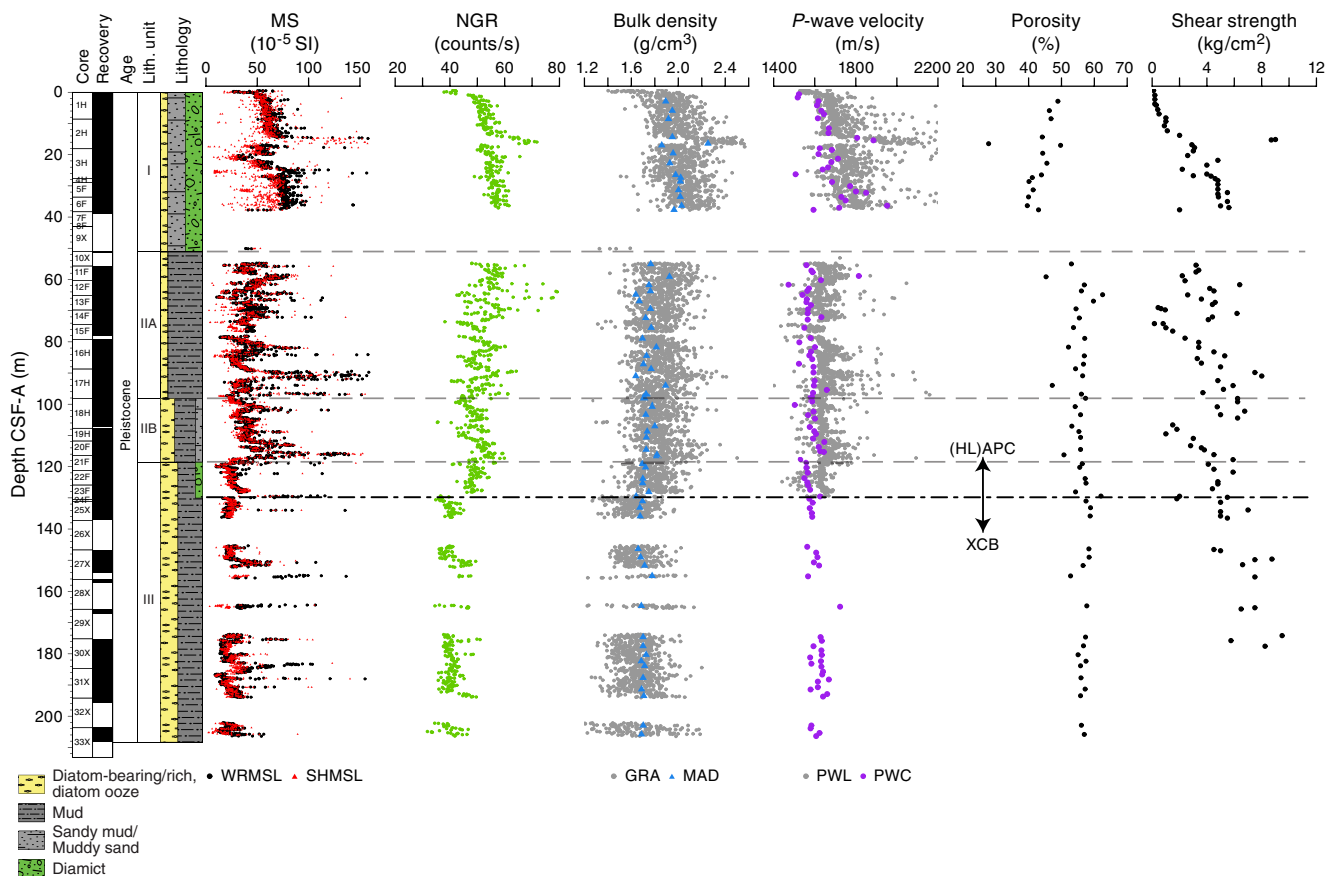

Figure F21. Physical properties summary, Hole U1525A. Dashed gray lines mark intervals with distinctive physical property characteristics that correlate with lithostratigraphic units (see Table T12).

Table T12. Physical properties by lithostratigraphic unit, Hole U1525A. MS = magnetic susceptibility, NGR = natural gamma radiation. **Download table in CSV format.**

| Unit/ Subunit	Top		Bottom		Physical properties	Basic description
	Core, section, interval (cm)	Depth CSF-A (m)	Core, section, interval (cm)	Depth CSF-A (m)		
	374-U1525A-		374-U1525A-			
I	1H-1, 0	0	10X-1, 11	51.11	MS: downhole increase (low in Cores 2H and 3H) NGR: downhole increase Bulk density: downhole increase *P*-wave: downhole increase Porosity: downhole decrease (low in Core 2H) Shear strength: downhole increase (peak in Core 2H)	Massive diatom-bearing sandy mud with dispersed clasts interbedded with clast-poor/rich muddy diamict
IIA	10X-1, 11	51.11	18H-1, 0	98.20	MS: low to moderate with overall downhole increase NGR: downhole decrease Bulk density: low to moderate with minor variability *P*-wave: low to moderate with minor variability Porosity: high with minor variability Shear strength: variable with overall downhole increase	Massive to laminated diatom-bearing mud interbedded with diatom-bearing sandy mud with dispersed clasts
IIB	18H-1, 0	98.20	21F-2, 58	118.58	MS: moderate with downhole increase NGR: moderate with slight downhole increase Bulk density: low to moderate with minor variability *P*-wave velocity: low to moderate with slight downhole increase Porosity: high with minor variability Shear strength: variable with overall downhole increase	Massive to laminated diatom-rich mud interbedded with diatom-rich sandy mud with dispersed clasts
III	21F-2, 58	118.58	33X-CC, 34	208.27	MS: low to moderate with variability NGR: low to moderate with minor variability Bulk density: moderate with minor variability *P*-wave: low to moderate with minor variability Porosity: high with minor variability Shear strength: variable with overall downhole increase	Massive to finely laminated muddy diatom ooze/diatom-rich mud interbedded with diatom-rich sand and diamict
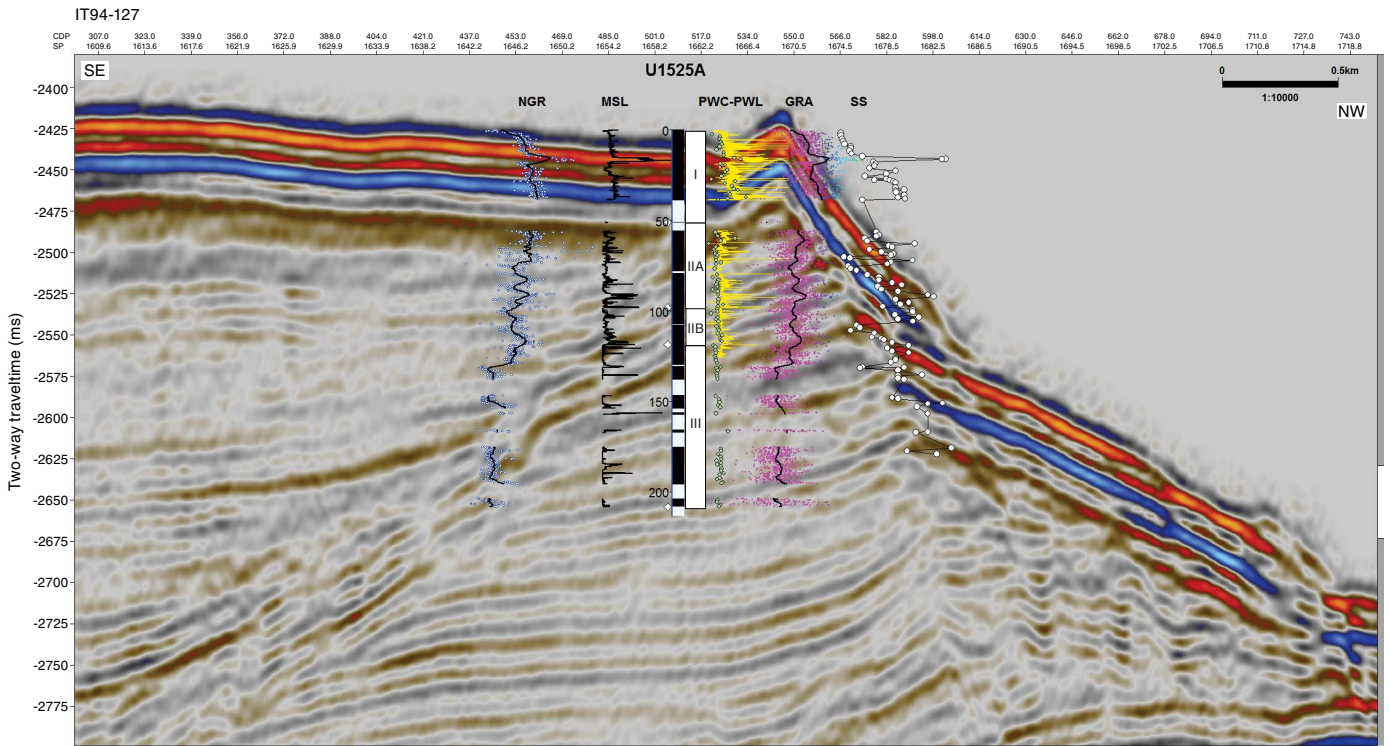
Figure F22. Core-seismic integration, Hole U1525A. Seismic-reflection Profile IT94AR-127 is a multichannel reflection seismic profile collected by Istituto Nazionale di Oceanografia e Geofisica Sperimentale (OGS, Italy) under Programma Nazionale delle Ricerche in Antartide (PNRA) in 1994 (Finetti et al., unpubl. data) with a 2 × 20 air gun (74.8 L). Data were acquired with a 1500 m streamer (120 channels; first offset = 164 m, last offset = 1664 m). Reprocessing for IODP Expedition 374 was made by Riccardo Geletti (OGS, unpubl. data). NGR = core NGR (counts/s), MSL = core MS (10⁻⁵ SI), PWC-PWL = archive-half and whole-round *P*-wave velocity (m/s), GRA = core bulk density (g/cm³), SS = shear strength (kg/cm²). CDP = common depth point.

with, an underlying sediment mound. The upper part of the mound recovered in Subunits IIA and IIB and Unit III is characterized by a stratified package of high-amplitude, subhorizontal reflectors that slightly dip toward the southeast (Figure **F22**). Hole U1525A was terminated before penetrating RSU3 (see **Operations**), which is inferred to be below the base of the hole. However, RSU2 was likely penetrated in Unit III.

7. Geochemistry and microbiology

Site U1525 samples were analyzed for headspace gas, interstitial water chemistry, and bulk sediment geochemistry. Headspace gas (methane and ethane) concentration is low in the upper ~120 m CSF-A and increases to 6640 and 7 ppmv, respectively, at ~194 m CSF-A. Interstitial water analyses of the mudline and 12 whole-round samples indicate biogeochemical zonation with sulfate reduction in the uppermost ~100 m CSF-A. Downhole variations in interstitial water elemental concentration (e.g., magnesium, calcium, silicon, and lithium) broadly correspond with lithologic changes and total organic carbon (TOC) and calcium carbonate ($CaCO_3$) content. TOC and carbonate contents are low (<1% and <5%, respectively). The highest and most variable carbonate content and TOC/total nitrogen (TN) ratios occur in the upper ~35 m CSF-A (lithostratigraphic Unit I).

7.1. Volatile hydrocarbons

Headspace gas analyses were performed at a resolution of one sample per core (9.6 m advance) or one sample every other core for HLAPC cores (4.8 m advance) throughout Hole U1525A (Cores 374-U1525A-1H through 33X; N = 21) as part of the routine environmental protection and safety monitoring program. Methane is the dominant hydrocarbon, and ethane is present in low concentration. Methane concentration is low (≤11 ppmv) in the upper 124.20 m CSF-A and increases from 11 ppmv at 124.20 m CSF-A to 6641 ppmv at 193.81 m CSF-A (Figure **F23**; Table **T13**). Ethane

Table T13. Volatile hydrocarbon concentrations, Hole U1525A. **Download table in CSV format.**
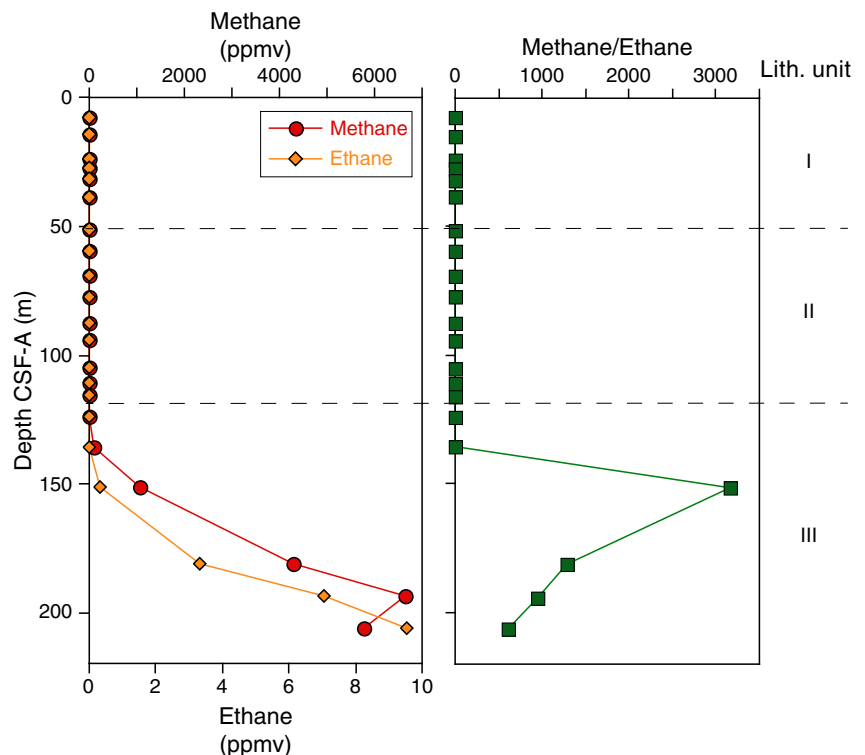

Figure F23. Headspace gas concentrations, Hole U1525A. Dashed lines mark lithostratigraphic unit boundaries (see Lithostratigraphy; Table T2).

concentration is below detection limit in the upper ~150 m CSF-A and increases to 10 ppmv at 206.37 m CSF-A (Figure **F23**). The methane/ethane ratio declines from 3162 at 151.21 m CSF-A to 608 at 206.37 m CSF-A (Figure **F23**).

7.2. Interstitial water chemistry

A total of 12 interstitial water samples were squeezed from 5 or 10 cm whole-round samples (Table **T14**) with a sampling resolution dictated by core recovery and lithology from 4.45 to 181.09 m CSF-A. Interstitial water sampling was not conducted deeper than 181.09 m CSF-A. An additional sample from the mudline was split and analyzed as a comparative sample for shipboard parameters and shore-based analyses.

7.2.1. Salinity, sulfate, sulfur, iron, manganese, alkalinity, and ammonium

Interstitial water salinity decreases from 35 at 4.45 m CSF-A to 33 at 181.09 m CSF-A. Water collected from the mudline of Site U1525 has a salinity of 36, and chloride, bromide, and sodium concentrations are higher than typical Ross Sea water. The mudline water likely reflects a mixture of in situ seawater and higher salinity water introduced by coring operations. Total sulfur and sulfate concentrations show identical downhole profiles. Sulfate decreases from >29 mM at the mudline, which is slightly elevated above typical seawater concentration, to close to the detection limit of inductively coupled plasma–optical emission spectroscopy (ICP-OES) deeper than ~130 m CSF-A (Figure **F24**). Iron concentration in the interstitial water is below the detection limit shallower than ~60 m CSF-A and at 94.35 and 181.09 m CSF-A. In most samples between 68.87 and 135.60 m CSF-A, iron was detected in interstitial water with concentrations up to ~5 μM. Manganese concentration is variable in the upper 31.85 m CSF-A from a very low value of 4 μM in the mudline sample to the highest value of 118 μM at 14.57 m CSF-A. From 59.43 m CSF-A, the manganese profile is better defined and shows a general decrease from 50 to 6 μM in the lowermost interstitial water sample (181.09 m CSF-A). Alkalinity increases nearly linearly from a low value of 2.5 mM in the mudline sample to 19.4 mM at 181.09 m CSF-A. This trend is paralleled by the ammonium concentration in interstitial water, which increases from ~6 μM in the mudline sample to 1017 μM at 181.09 m CSF-A (Figure **F24**).

Table T14. Interstitial water geochemical data, Hole U1525A. **Download table in CSV format.**
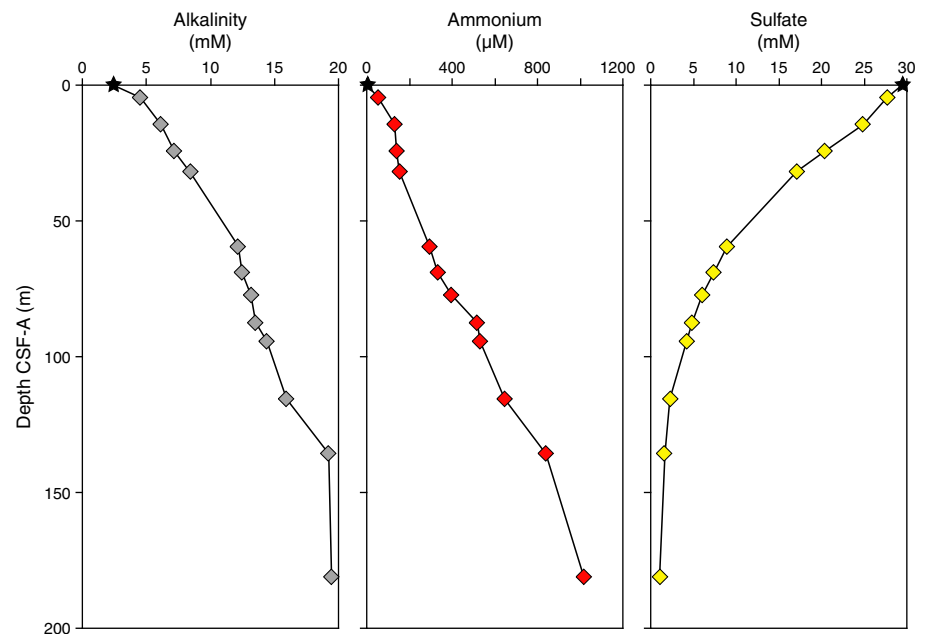

Figure F24. Interstitial water alkalinity, ammonium, and sulfate, Hole U1525A. Stars = mudline water concentrations.

Downhole increase in ammonium concentration is likely the result of mineralization of organic carbon and is possibly associated with the anaerobic oxidation of methane by microbial activity. All downhole profiles described above are consistent with manganese and sulfate reduction in the suboxic to anoxic transition zone.

7.2.2. Lithium, calcium, magnesium, and silicon

Systematic downhole variability is observed for magnesium (34%), calcium (34%), and potassium (36%) (Figure **F25**). In detail, magnesium concentration decreases slightly downhole from 53 to 44 mM in the uppermost ~32 m CSF-A to an average concentration of 40 ± 1 mM from 59.43 to 135.60 m CSF-A (Figure **F25**). The bottommost sample shows slightly decreased magnesium concentration (35 mM). Calcium concentration exhibits a very smooth profile with values in the uppermost ~32 m CSF-A between 10 and 11 mM. Calcium concentration decreases linearly to 7 mM between 59.43 and 94.35 m CSF-A and remains essentially constant downhole to 181.09 m CSF-A (Figure **F25**). The lithium profile shows some similarities to downhole trends in calcium but also some deviations; lithium decreases in the uppermost ~32 m CSF-A from 30 µM in the mudline water sample to 19 µM at 31.85 m CSF-A. Deeper than 59.43 m CSF-A, lithium concentration more than doubles along a linear trend from 23 to 59 µM. Silicon concentration in interstitial water shows the closest relationship to lithostratigraphic units, with a peak value of 1006 µM at 77.32 m CSF-A possibly associated with higher biogenic silica (diatom) dissolution in the diatombearing mud of lithostratigraphic Subunit IIA (see **Lithostratigraphy**). Overall, silicon concentration increases from 169 µM in the mudline sample to 578 µM in the first interstitial water sample at 4.45 m CSF-A. Deeper than 14.57 m CSF-A, silicon concentration varies between 666 and 1006 µM, likely reflecting downhole changes in interstitial water silica saturation, which approaches equilibrium conditions at ~1000 µM (Figure **F25**).
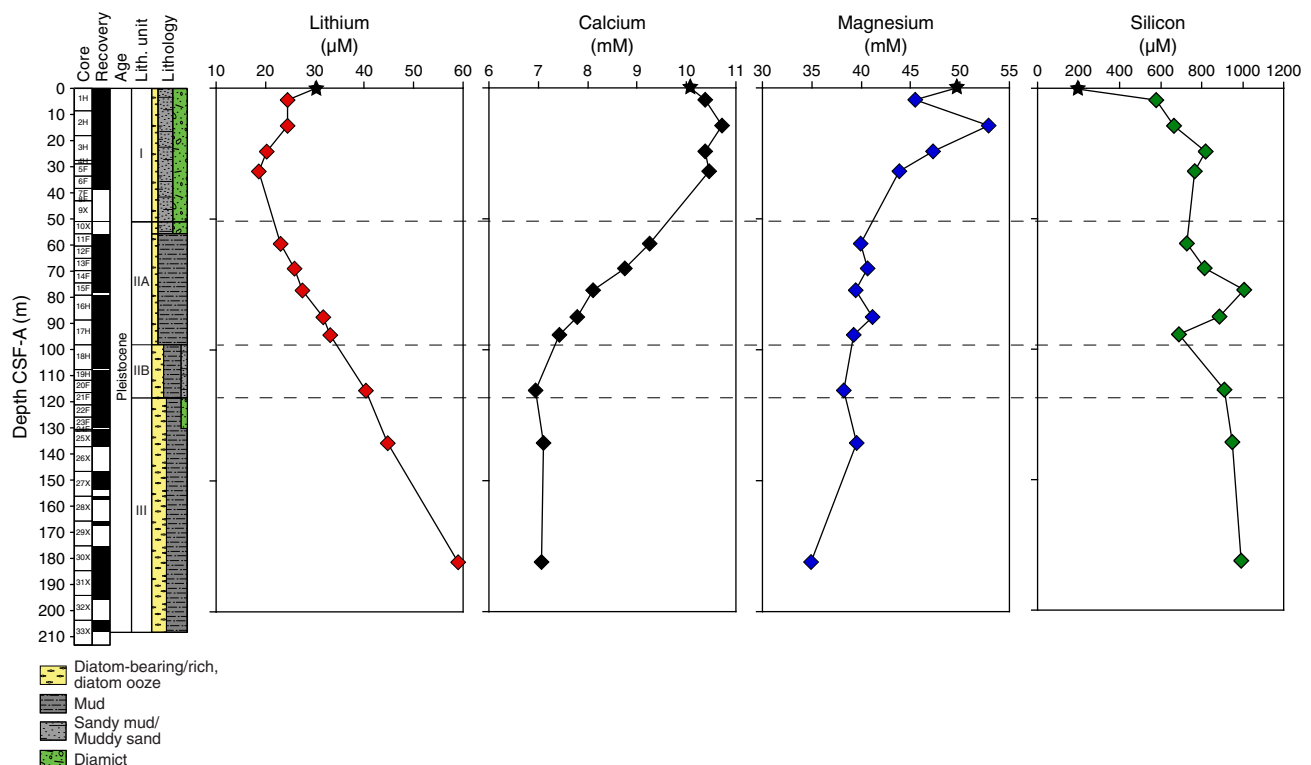

Figure F25. Interstitial water lithium, calcium, magnesium, and silicon, Hole U1525A. Stars = mudline water concentrations. Dashed lines mark lithostratigraphic unit boundaries (see Lithostratigraphy; Table T2).

7.3. Bulk sediment geochemistry

7.3.1. Carbon, nitrogen, and carbonate

A total of 47 sediment samples from the major lithostratigraphic units identified at Site U1525 were analyzed for total carbon, TN, and total inorganic carbon (Table **T15**). TOC and $CaCO_3$ contents were subsequently calculated. TOC content is generally low (<0.6 wt%; Figure **F26**) and increases from minimum values (<0.2 wt%) in the upper 35 m CSF-A to maximum values (0.3–0.6 wt%) in the diatom-rich mud and sandy diamict of lithostratigraphic Units II and III between 68.46 and 206.89 m CSF-A (see **Lithostratigraphy**). TN content is very low (≤0.05 wt%) but increases downhole. Except for two samples from Sections 374-U1525A-6F-3 and 19H-1, the TOC/TN ratio ranges between 1 and 11 (Figure **F26**). These values are relatively low compared with those observed at continental shelf Sites U1521–U1523 and suggest a reduced input of terrigenous-derived organic matter at Site U1525. $CaCO_3$ content is generally low, from 0.1 to 4.5 wt% (Figure **F26**). Slightly higher values (>2 wt%) are observed exclusively in the sandy mud and diamict of Unit I in the upper 34 m CSF-A. Although $CaCO_3$ content is lower in the diatom-bearing to diatom-rich mud of Unit II (see **Lithostratigraphy**), it is also notably variable, with concentrations fluctuating between 0.1 and 1.5 wt%.

7.4. Microbiological sampling

In total, 20 samples for shore-based stable and clumped isotope analyses of methane and ethane were collected from Sections 374-U1525A-1H-4 through 33X-2. Additional samples for detailed analyses of metagenomics, cell counts, metabolomics, and cultures were taken from Cores 3H, 11F, 16H, and 20F (see **Geochemistry and microbiology** in the Expedition 374 methods chapter [McKay et al., 2019a] for details).
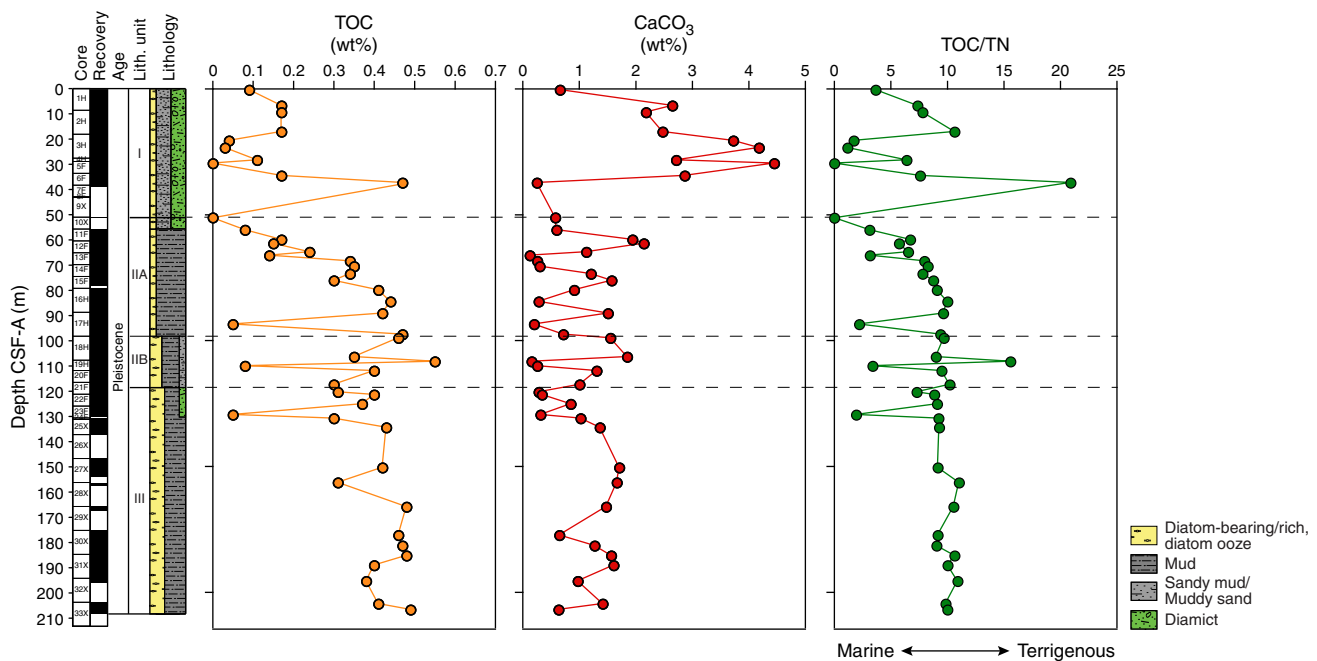
Table T15. Bulk sediment carbon, nitrogen, and total organic carbon (TOC)/total nitrogen (TN), Hole U1525A. **Download table in CSV format.**

Figure F26. Bulk sediment TOC, calcium carbonate ($CaCO_3$) and TOC/TN ratio, Hole U1525A. Dashed lines mark lithostratigraphic unit boundaries (see Lithostratigraphy; Table T2).

8. References

Arndt, J.E., Schenke, H.W., Jakobsson, M., Nitsche, F.O., Buys, G., Goleby, B., Rebesco, M., et al., 2013. The International Bathymetric Chart of the Southern Ocean (IBCSO) Version 1.0—a new bathymetric compilation covering circum-Antarctic waters. *Geophysical Research Letters,* 40(12):3111–3117. **https://doi.org/10.1002/grl.50413**

Bergamasco, A., Defendi, V., Zambianchi, E., and Spezie, G., 2002. Evidence of dense water overflow on the Ross Sea shelf-break. *Antarctic Science,* 14(3):271–277. **https://doi.org/10.1017/S0954102002000068**

Bjørklund, K.R., and Kruglikova, S.B., 2003. Polycystine radiolarians in surface sediments in the Arctic Ocean basins and marginal seas. *Marine Micropaleontology,* 49(3):231–273. **https://doi.org/10.1016/S0377-8398(03)00036-7**

Esper, O., and Zonneveld, K.A.F., 2002. Distribution of organic-walled dinoflagellate cysts in surface sediments of the Southern Ocean (eastern Atlantic sector) between the Subtropical Front and the Weddell Gyre. *Marine Micropaleontology,* 46(1–2):177–208. **https://doi.org/10.1016/S0377-8398(02)00041-5**

Esper, O., and Zonneveld, K.A.F., 2007. The potential of organic-walled dinoflagellate cysts for the reconstruction of past sea-surface conditions in the Southern Ocean. *Marine Micropaleontology,* 65(3–4):185–212. **https://doi.org/10.1016/j.marmicro.2007.07.002**

Florindo, F., Farmer, R.K., Harwood, D.M., Cody, R.D., Levy, R., Bohaty, S.M., Carter, L., and Winkler, A., 2013. Paleomagnetism and biostratigraphy of sediments from Southern Ocean ODP Site 744 (southern Kerguelen Plateau): implications for early-to-middle Miocene climate in Antarctica. *Global and Planetary Change,* 110(C):434–454. **https://doi.org/10.1016/j.gloplacha.2013.05.004**

Gradstein, F.M., Ogg, J.G., Schmitz, M.D., and Ogg, G.M. (Eds.), 2012. *The Geological Time Scale 2012:* Amsterdam (Elsevier). **https://doi.org/10.1016/C2011-1-08249-8**

McKay, R.M., De Santis, L., Kulhanek, D.K., Ash, J.L., Beny, F., Browne, I.M., Cortese, G., Cordeiro de Sousa, I.M., Dodd, J.P., Esper, O.M., Gales, J.A., Harwood, D.M., Ishino, S., Keisling, B.A., Kim, S., Kim, S., Laberg, J.S., Leckie, R.M., Müller, J., Patterson, M.O., Romans, B.W., Romero, O.E., Sangiorgi, F., Seki, O., Shevenell, A.E., Singh, S.M., Sugisaki, S.T., van de Flierdt, T., van Peer, T.E., Xiao, W., and Xiong, Z., 2019a. Expedition 374 methods. *In* McKay, R.M., De Santis, L., Kulhanek, D.K., and the Expedition 374 Scientists, *Ross Sea West Antarctic Ice Sheet History.* Proceedings of the International Ocean Discovery Program, 374: College Station, TX (International Ocean Discovery Program). **https://doi.org/10.14379/iodp.proc.374.102.2019**

McKay, R.M., De Santis, L., Kulhanek, D.K., Ash, J.L., Beny, F., Browne, I.M., Cortese, G., Cordeiro de Sousa, I.M., Dodd, J.P., Esper, O.M., Gales, J.A., Harwood, D.M., Ishino, S., Keisling, B.A., Kim, S., Kim, S., Laberg, J.S., Leckie, R.M., Müller, J., Patterson, M.O., Romans, B.W., Romero, O.E., Sangiorgi, F., Seki, O., Shevenell, A.E., Singh, S.M., Sugisaki, S.T., van de Flierdt, T., van Peer, T.E., Xiao, W., and Xiong, Z., 2019b. Expedition 374 summary. *In* McKay, R.M., De Santis, L., Kulhanek, D.K., and the Expedition 374 Scientists, *Ross Sea West Antarctic Ice Sheet History.* Proceedings of the International Ocean Discovery Program, 374: College Station, TX (International Ocean Discovery Program). **https://doi.org/10.14379/iodp.proc.374.101.2019**

McKay, R.M., De Santis, L., Kulhanek, D.K., Ash, J.L., Beny, F., Browne, I.M., Cortese, G., Cordeiro de Sousa, I.M., Dodd, J.P., Esper, O.M., Gales, J.A., Harwood, D.M., Ishino, S., Keisling, B.A., Kim, S., Kim, S., Laberg, J.S., Leckie, R.M., Müller, J., Patterson, M.O., Romans, B.W., Romero, O.E., Sangiorgi, F., Seki, O., Shevenell, A.E., Singh, S.M., Sugisaki, S.T., van de Flierdt, T., van Peer, T.E., Xiao, W., and Xiong, Z., 2019c. Site U1524. *In* McKay, R.M., De Santis, L., Kulhanek, D.K., and the Expedition 374 Scientists, *Ross Sea West Antarctic Ice Sheet History.* Proceedings of the International Ocean Discovery Program, 374: College Station, TX (International Ocean Discovery Program). **https://doi.org/10.14379/iodp.proc.374.106.2019**

Nishimura, A., Nakaseko, K., and Okuda, Y., 1997. A new coastal water radiolarian assemblage recovered from sediment samples from the Antarctic Ocean. *Marine Micropaleontology,* 30(1–3):29–44. **https://doi.org/10.1016/S0377-8398(96)00019-9**

Orsi, A.H., and Wiederwohl, C.L., 2009. A recount of Ross Sea waters. *Deep Sea Research, Part II: Topical Studies in Oceanography,* 56(13–14):778–795. **https://doi.org/10.1016/j.dsr2.2008.10.033**

Osterman, L.E., and Kellogg, T.B., 1979. Recent benthic foraminiferal distributions from the Ross Sea, Antarctica: relation to ecologic and oceanographic conditions. *Journal of Foraminiferal Research,* 9(3):250–269. **https://doi.org/10.2113/gsjfr.9.3.250**

Schröder-Ritzau, A., 1995. Aktuopaläontologische Untersuchung zu Verbreitung und Vertikalfluß von Radiolarien sowie ihre räumliche und zeitliche Entwicklung im Europäischen Nordmeer. *Berichte aus dem Sonderforschungsbereich 313, Veränderungen der Umwelt - Der Nördliche Nordatlantik:* Kiel, Germany (Christian-Albrechts-Universität), 52. **https://doi.org/10.2312/reports-sfb313.1995.52**

Swanberg, N.R., and Eide, L.K., 1992. The radiolarian fauna at the ice edge in the Greenland Sea during summer, 1988. *Journal of Marine Research,* 50(2):297–320. **https://doi.org/10.1357/002224092784797674**

Whitworth, T., III, Orsi, A.H., Kim, S.-J., Nowlin, W.D., Jr., and Locarnini, R.A., 1995. Water masses and mixing near the Antarctic slope front. *In* Jacobs, S.S., and Weiss, R.F. (Eds.), *Antarctic Research Series* (Volume 75): *Ocean, Ice, and Atmosphere: Interactions at the Antarctic Continental Margin:* Washington, DC (American Geophysical Union), 1–27. **http://onlinelibrary.wiley.com/doi/10.1029/AR075p0001/summary**

Zonneveld, K.A.F., Marret, F., Versteegh, G.J.M., Bogus, K., Bonnet, S., Bouimetarhan, I., Crouch, E., et al., 2013. Atlas of modern dinoflagellate cyst distribution based on 2405 data points. *Review of Palaeobotany and Palynology,* 191. **https://doi.org/10.1016/j.revpalbo.2012.08.003**